INL/RPT-23-74941

Multiscale and Machine Learning Modeling for Additive Manufacturing

September 29, 2023

Sudipta Biswas[1], Somayajulu L. N. Dhulipala[1], Peter German[1], Alexander D. Lindsay[1], Matthew D. Eklund[1], Danny Hermawan[2], Hongsup Oh[3], Wen Jiang[1,4], and Andrea M. Jokisaari[1]

[1]*Nuclear Science and Technology, Idaho National Laboratory*
[2]*Materials Engineering, Purdue University*
[3]*Mechanical Engineering, University of Utah*
[4]*Nuclear Engineering, North Carolina State University*

INL is a U.S. Department of Energy National Laboratory
operated by Battelle Energy Alliance, LLC

INL/RPT-23-74941

Multiscale and Machine Learning Modeling for Additive Manufacturing

Sudipta Biswas[1], Somayajulu L. N. Dhulipala[1], Peter German[1], Alexander D. Lindsay[1], Matthew D. Eklund[1], Danny Hermawan[2], Hongsup Oh[3], Wen Jiang[1,4], and Andrea M. Jokisaari[1]

[1]**Nuclear Science and Technology, Idaho National Laboratory**
[2]**Materials Engineering, Purdue University**
[3]**Mechanical Engineering, University of Utah**
[4]**Nuclear Engineering, North Carolina State University**

September 29, 2023

Idaho National Laboratory
Idaho Falls, Idaho 83415

http://www.inl.gov

Prepared for the
U.S. Department of Energy
Office of Nuclear Energy
Under DOE Idaho Operations Office
Contract DE-AC07-05ID14517

Page intentionally left blank

SUMMARY

Additive manufacturing (AM) techniques provide the opportunity to simultaneously design new materials and components with complex structures in less time, enabling faster material developments. Even though compositionally similar, the texture of the materials produced by such techniques is significantly different from conventionally manufactured materials. Additively manufactured materials produces highly heterogeneous microstructure within a single build. Such variations in the microstructure make qualifying AM products challenging for extreme environment applications. Understanding the AM process and its influence on the materials' microstructures/properties is paramount for evaluating the workability and performance of the manufactured materials.

The performance of AM materials for advanced nuclear reactor applications is of interest to the Advanced Materials and Manufacturing Technologies (AMMT) program under the Department of Energy Office of Nuclear Energy. Hence, considering the microstructural variabilities in the AM products and their impact on the performance of the material, it is important to correlate the process conditions to the final product and establish a process-structure-property-performance (PSPP) correlation for AM materials. Conventionally, *in-situ* and *ex-situ* characterizations and testing are performed to correlate different aspects of the AM process to the final product and its performance. However, adopting a trial-and-error approach to experimentally evaluate the vast range of process parameters required to capture the microstructural variabilities is cost-prohibitive. Modeling and simulation provide a comparatively inexpensive way to understand and correlate the microstructural evolution to the processing conditions.

The melting and subsequent solidification that occurs during the AM process is a complex phenomenon that requires multiscale multiphysics analysis. Idaho National Laboratory's (INL) Multiphysics Object-Oriented Simulation Environment (MOOSE), specifically the MOOSE Application Library for Advanced Manufacturing UTilitiEs (MALAMUTE) software, provides an ideal platform for developing the multiphysics multiscale model to explore the intricacies of the microstructural evolution during the AM processes within a single framework. Furthermore, given that such full-fidelity simulations can be computationally intensive, reduced order models are necessary to explore the PSPP space for AM materials in an efficient, reliable, and cost-effective way.

The AMMT program aims to demonstrate its new accelerated development and qualification methods via laser powder bed fusion 316 stainless steel to aid the understanding of the the process variabilities on its performance under nuclear

environments. Here, we lay the foundation to integrate multiscale mechanistic models with machine learning approaches for additively manufactured 316L stainless steel. We utilize and extend the existing capabilities of MOOSE and MALAMUTE to develop a multiscale model that can couple different physical aspects of the AM process in a modular way. This year, the necessary modeling capabilities and the computational frameworks are developed with an ultimate goal of establishing the PSPP correlation for AM. A multiphysics multiscale model is developed using level-set and Arbitrary Lagrangian Eulerian (ALE) approach to demonstrate the melt pool dynamics during the laser powder bed fusion method. A phase-field-based microstructural evolution model is developed to capture the solidification and epitaxial grain growth under moving heat source in 316L SS. The model demonstrates the elongated grain formation and Cr segregation observed in typical additively manufactured SS materials. Furthermore, various machine learning models are developed to simplify the outputs of the physics-based models and represent them with a simplified surrogate model. A genetic programming-based symbolic regression model is developed to correlate the process conditions to the cooling rate of the work-piece. In addition, a Proper Orthogonal Decomposition based dimensionality reduction workflow and a multi-output Gaussian processes model has been implemented in the Multiphysics Object-Oriented Simulation Environment (MOOSE). For initial verification, the models have been tested for efficiently predicting the temperature distribution surrounding the melt pool.

This work can capture the microstructural variabilities that are often missing in the part-scale models. In fiscal year 2023, several unique modeling capabilities have been developed and tested to capture material evolution during the AM process. In the following years, MALAMUTE will be used to connect different aspects of the models and quantitatively predict the microstructural evolution. The developed ML-based surrogate model will consider the process conditions as the input to predict the microstructural features in a cost-effective way. Furthermore, with uncertainty quantification a synergistic framework will be established to demonstrate active learning for material evolution during AM. Additionally, the generated microstructures can be used by other work packages under AMMT to evaluate the properties and environmental response of the material at the mesoscale. Thus, this work help identify the key microstructural features that are significant in property/performance prediction of the AM products. This work will provide inputs to the large-scale process variability models to reevaluate and validate assumptions/simplifications made in the part-scale models. Furthermore, through active learning this work will help identify the data need from both modeling and experimental sides for development of a robust digital twin for AM.

ACKNOWLEDGEMENTS

This report has been funded by the Advanced Materials and Manufacturing Technologies (AMMT) program within the U.S. Department of Energy Office of Nuclear Energy. This research made use of the resources of the High Performance Computing Center at Idaho National Laboratory, which is supported by the Office of Nuclear Energy of the U.S. Department of Energy and the Nuclear Science User Facilities under Contract No. DE-AC07-05ID14517. This manuscript has been authored by Battelle Energy Alliance, LLC under Contract No. DE-AC07-05ID14517.

Page intentionally left blank

CONTENTS

FIGURES

TABLES

ACRONYMS

ALE	Arbitrary Lagrangian Eulerian
MALAMUTE	MOOSE Application Library for Advanced Manufacturing UTilitiEs
MOOSE	Multiphysics Object-Oriented Simulation Environment
PETSc	Portable Extensible Toolkit for Scientific Computation
POD	Proper Orthogonal Decomposition
STM	Stochastic Tools Module

Page intentionally left blank

1. Introduction

In recent years, additive manufacturing (AM) techniques have gained significant interest across government agencies and nuclear industries due to their ability to produce complex structures in a shorter time, facilitating faster material developments. These techniques have the potential to change the paradigm of new material and component designs for nuclear applications, such as producing new alloys and graded materials, as well as innovative component designs for advanced nuclear reactors [7]. Advanced materials and manufacturing technologies (AMMT) program under the Department of Energy (DOE) Office of Nuclear Energy (NE) aims to accelerate the development and qualification of AM materials for nuclear applications. Several work packages under the program focuses on how the AM products perform under extreme thermal and irradiation conditions. However, an understanding of the initial microstructure to begin with is pivotal to evaluate the performance of the material and eventually qualify it for advanced nuclear reactors.

The key challenge AM techniques face is controlling process conditions to obtain desired microstructures and properties for targeted applications. AM also faces the issue of reproducibility due to microstructural and property variation across, as well as within, builds. For example, depending on the build direction, the texture of the AM sample could be very heterogeneous, leading to extremely anisotropic strength and deformation behavior [8–10]. Compared to traditional manufacturing techniques, qualifying AM products for extreme environments becomes challenging due to such morphology variations from build to build and even within a single build [11]. This is especially true for novel material development for nuclear applications. It is therefore of utmost importance to understand the microstructural evolution during the manufacturing process and optimize the process parameters to design materials with the desired microstructures and properties.

Various experimental and computational efforts have been devoted to establishing a process-structure-property-performance (PSPP) relation for various AM processes. Experimentally, *in-situ* observations and *ex-situ* characterizations and testing have been performed to correlate different aspects of the AM process to the final product and its performance. For example, recently, the effects of processing parameters on the solidification textures were evaluated and an attempt was made to control texture during the electron beam melting process [4]. However, adopting a trial-and-error approach to experimentally evaluate the process parameters required for texture control is expensive. Modeling and simulation provide a cost-effective way to understand and correlate the microstructural evolution to the processing conditions. The melting and subsequent solidification that occurs during the AM process is a complex phenomenon that requires multiscale multiphysics analysis. Several macroscopic studies have been done to capture the heat and fluid flow during various AM processes as well as part-scale component modeling [12]. However, physics-based microstructural analysis of the material undergoing the process is limited [13]. Specifically, physics-based models to predict the microstructural evolution including grain formation and chemical segregation during AM processes are currently lacking in the

literature. Moreover, so far, the modeling efforts have been focused on developing and utilizing different tools to simulate different aspects of the AM process. These efforts are disjointed and rarely can be utilized in conjunction with each other to explore the vast PSPP space. Alternatively, considering that full-fidelity multiphysics models are computationally expensive, surrogate models have emerged that again depend on the availability and quality of experimental data and are limited in terms of the underlying physics they capture [14, 15].

Idaho National Laboratory's (INL) Multiphysics Object-Oriented Simulation Environment (MOOSE), specifically the MOOSE Application Library for Advanced Manufacturing UTilitiEs (MALAMUTE) software, provides an ideal platform for developing the multiphysics multiscale model to explore the intricacies of the microstructural evolution during the AM processes within a single framework. This work package aims to develop a MOOSE-based multiscale model that can couple different physical aspects of the AM process in a modular way. Here, we utilize and extend the existing capabilities of MOOSE and MALAMUTE to capture different aspects of the AM process. The physics-based process models captures the evolution of the melt pool. The microstructural evolution model captures the epitaxial grain growth under a moving heat source and associated chemical segregation in 316L stainless steel (SS). Furthermore, a machine learning (ML) framework is developed using MOOSE-based Stochastic Tool Module (STM) to generate a reduced-order surrogate model for correlating the process parameters to the final microstructure. In fiscal year 2023, the primary focus has been on developing the initial frameworks and models necessary for connecting the process conditions to the grain structure formed during the AM process.

The rest of the report is organized as follows. In Section 2 we present a short literature review to evaluate the role of various process parameters on the material behavior. This is done to identify the key parameters and conditions that the computational model developments should focus on. In Section 3.1 we present the process modeling capabilities of MALAMUTE and development of a phase-field model for capturing the associated grain growth and microsegregation in 316 SS. Finally, Section 4 presents the machine learning models necessary for deriving the reduced order models.

2. PSPP requirements for 316 SS

There are two broad categories of technologies in AM: laser powder bed fusion (LPBF) and directed energy deposition (DED), also known as beam deposition (BD) [16]. LPBF and DED are different yet complimentary processes, each with pros and cons. During both the process, the target material is heated to create a melt pool which solidifies to build a designed part. The primary difference between LPBF and DED is the source of the added material. LPBF creates a manufactured product by heating a powder bed in layers where a new layer of powder is continuously spread to the target, whereas the added material for DED is typically supplied in the form of a wire or powder which is then heated and deposited on the material surface. Several advantages of DED over LPBF include better static and dynamic properties of the manufactured material in the as-deposited condition versus PBF-deposited parts, high deposition rates, larger part sizes, a higher technology readiness level (TRL), and larger particle sizes which improves cost and safety. Some disadvantages of DED versus LPBF include a lower-dimensional resolution with larger waviness on the surface, higher surface roughness in blown powder systems, the requirement of post-fabrication machining, and lower powder efficiency and powder recyclability especially when using a composite powder mixture [17].

In AM, process parameters are those inputs that influence and control the amount and rate of energy deposited to the work piece to build a new component. This typically results in distinguished material composition and properties leading to nonuniform distribution of elements and composition of the material, and anisotropic grain characteristics such as size, shape, and distribution, etc. [1]. Hence, AM requires optimizing process parameters to produce specific material microstructures with the goal of achieving the desired material properties of the final manufactured product. Several of these desirable material properties include the material density, porosity, yield strength, tensile strength, resilience to radiation damage, etc., which are chosen depending on the application for the material. In the remainder of this section, a review of PSPP for the additive manufacturing of various metals and alloys, with particular emphases on stainless steels (SS), is given. The primary processing parameters considered are laser power and laser scanning speeds, and their effects on the structure and material properties of SS produced through AM are examined.

2.1 Effect of laser power

Laser power, P, has a direct effect on the amount of energy deposited to a surface or powder during the melting process. The energy density Q can be related to the laser power, laser beam spot size d, scanning speed v, and coupling efficiency η [1],

$$Q = \frac{\pi \eta P}{4hdv} \tag{1}$$

The fraction of overlap between two laser passes is defined as,

$$O = \frac{d}{h}, \tag{2}$$

where h is the scan line spacing. The energy delivered per volume for each laser track $\bar{Q}$ for a single layer of powder with thickness w is then calculated as,

$$\bar{Q} = \frac{\pi \eta P}{4hvw} \tag{3}$$

Simchi [1] defined the specific energy input ψ as the total energy per volume delivered to each track in the sample. This is defined as,

$$\psi = \frac{P}{hvw} \tag{4}$$

Simchi confirmed by experiments that porosity decreases in various samples as energy input increases due to either higher laser power P or lower scan rate v. In general, parts produced using LPBF result in different mechanical properties along various directions. This was shown in Inconel 718 samples examined by Amato et. al [18] to be a result of the anisotropic arrangement of the dendritic microstructure observed in the components. A higher laser energy density via slower scan speed, smaller hatch spacing, smaller layer thickness, and higher laser power produced improved densification in various ferrous metal powders [1]. Miranda et al. [19] also confirmed that higher laser power results generally in higher density, better microhardness, and higher strength. Li et al. [2] found that atomized 316L SS powder has a smoother molten surface and higher density given that there is a higher laser power and thinner layer thickness used in the process. Kong et al. [20] found that 316L SS formed with higher laser powers showed improved elongation, corrosion resistance, and biocompatibility.

However, some studies demonstrate that there can be a deleterious effect to using excessively high laser powers. While higher energy density generally results in lower porosity, a study of 316L SS by Wang et al. [21] showed that higher laser energy density can result in undercooling of the melt pool and an increase in grain size as well as primary dendrite spacing. Wang et al. concluded that there is a critical value below which increasing energy density results in an increase in microhardness and above which the microhardness decreases. This study found that too low of an energy density resulted in higher porosity, and rough surface quality of the samples. These results support the caveat that the appropriate energy density must be applied to each material to produce the desired material properties. The study by Choong et al. [22] showed that very high laser power deteriorates the mechanical properties of material samples due to vaporization of the molten material.

Simchi [1] also confirmed that smaller mean particle size and shorter scan length resulted in higher densification. The densification and microstructural evolution of AM parts with various powders including combinations of iron, copper, carbon, and phosphorous, as well as 316L SS and M2 high-speed steel were examined in that study. A simple sintering model was created based on

a first-order kinetics model for the change in void fraction, ϵ, according to time,

$$\frac{\partial \epsilon}{\partial t} = -k^{'} * \epsilon \tag{5}$$

where $k^{'}$ is the sintering rate and where the change in void fraction has its lower and upper boundaries $\epsilon_b \leq \epsilon \leq \epsilon_s$, where ϵ_b is the void fraction of the powder bed before sintering and ϵ_s is the minimum attained porosity in the sintered part. The densification factor, D, is defined as,

$$D = \frac{(\epsilon - \epsilon_b)}{(\epsilon_s - \epsilon_b)} \tag{6}$$

This was used to relate densification to specific energy input,

$$\ln(1 - D) = -K\psi \tag{7}$$

where K is the "densification coefficient" where powder melting occurs. A higher K coefficient, and hence a corresponding sharper positive slope on a $-\ln(1-D)$ versus ψ plot, indicates that there is less densification during the process. Figure 1 shows the comparison of experiments reported by Simchi as compared to this theory which shows excellent agreement. The results demonstrate that the densification is strongly correlated to the materials as well as to the specific energy input. The M2 high-speed steel had the highest densification coefficient of 28.3 which showed that this powder did not densify significantly after sintering. Adding 4 wt.% copper to the iron sample decreased the densification coefficient from 18.1 to 11.9, demonstrating that copper content has a significant effect on densification compared to pure iron. SS 316L with a calculated K=12.6 showed higher densification as compared to the other ferrous alloys tested in that study with the exception of the Fe-4Cu alloy having a comparable densification.

2.2 Effect of scanning speed

Here we present the effect of scanning speeds on various metals. According to a study of 316L SS by Simmons et al. [23], scanning speeds above the point of a critical value resulted in a degradation in mechanical properties due to excessive porosity in the material. Liu et al. [2] varied both scanning speeds and laser power between 800 to 1,000 mm/s and 185 to 245 W, respectively to capture the effects on microstructure of as fabricated 316L SS. Figure 2 shows electron backscatter diffraction (EBSD) maps (a and b in the figure), inverse pole figures (c and d in the figure), and grain boundary information (e and f in the figure) for samples fabricated using scanning speeds of 800 mm/s (a, c, and e in the figure) and 1000 mm/s (b, d, and f in the figure). The study showed that scanning speed had an effect on the melting pool boundaries, residual pores, solidification cells, nano-inclusions, grain size, and distributions in the sample material. The ultimate tensile strength (UTS) decreased slightly with an increase in energy density due to higher laser power and/or lower scanning speeds. An ultimate tensile strength of 707 MPa was

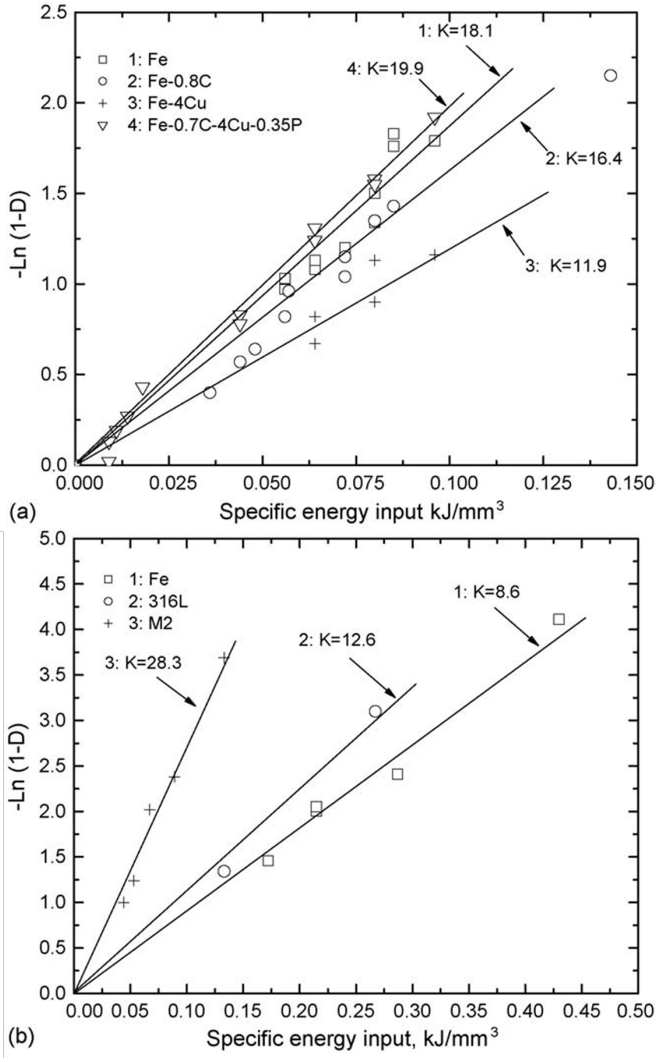

Figure 1: Simchi study on densification factor, D, versus specific energy input, ψ, of various ferrous alloys and M2 high-speed steel [1].

achieved at the higher 1000 mm/s scanning speed while maintaining good ductility with a total elongation of 30 percent. This higher ultimate tensile strength was attributed to the finer cellular structures and grains with a high number of low-angle grain boundaries (LAGBs) impeding the movement of dislocations through grain boundaries (HAGBs).

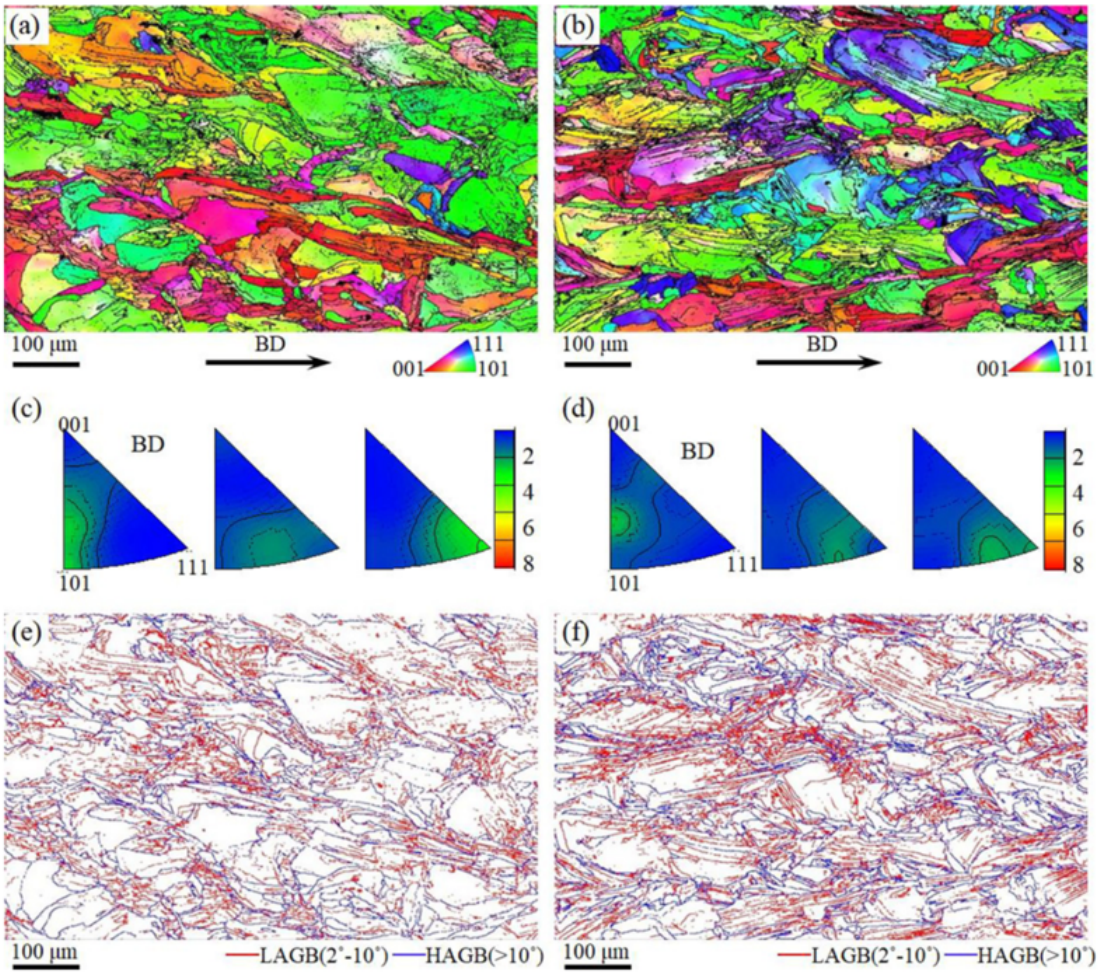

Figure 2: Examination of the effects on microstructure of 316L SS from Liu et al. [2]. EBSD orientation maps (a, b), inverse pole figures (c, d), and grain boundaries (e, f) for samples fabricated with scanning speeds of 800 mm/s (a, c, and e) and 1000 mm/s (b, d, and f).

A study by Chai et al. [3] was done to attempt to form 304 SS powder coating samples through laser additive manufacturing (LAM) using 2.5 kW laser power and scanning speeds ranging from 4 to 16 mm/s. Figure 3 shows a diagram of the sampling areas in the sample used in the determination of the iron-to-chromium (or Fe/Cr) ratios in the material. These results in the study show that the dilution rate and Fe/Cr ratio generally decreased in the cladding zone (CZ), heat affected zone (HAZ), and dilution zone (DZ) with increasing scan speed. The grain growth was also shown to be oriented toward the building direction of the cladding layer. It was also found that increasing the scanning speed caused crystal spacing of columnar crystals in the middle and

bottom layer to decrease gradually from 13.3 to 9.2 microns.

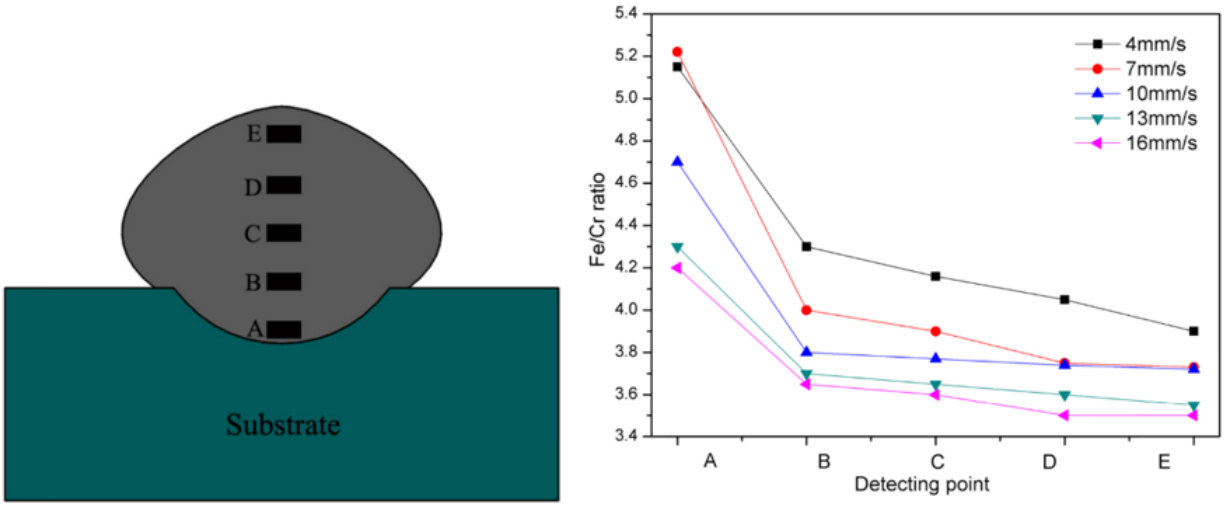

Figure 3: Left: diagram of sampling areas. Right: Fe/Cr ratios for sampling areas (corresponding to the left) in cladding area as a function of scanning speed [3].

Figure 4 shows the results of a study of the CZ microhardness as a function of scanning speed. It was determined based on these results that the hardness of the CZ gradually increased with scanning speed. This effect is due to the correlation between hardness and the cooling rate; the higher scan speed decreases laser residence time which resulted in lower melt pool temperatures and increased cooling rates. This faster cooling time resulted in a finger grain structure and more grain boundaries for an increased microhardness. As a function of distance from the substrate surface (the vertical axis on the left of Figure 4), the hardness of CZ increased because the material grain size gradually decreased for the same factor.

In the same study by Chai et al. [3], the microstructure of a single-pass cladding layer on different observation surfaces was examined in various directions. Figure 5 shows the sample diagram and three observation surfaces for a sample. This study revealed the growth of columnar crystals perpendicular to the substrate surface in the cladding layer. There were equi-axial crystals at the top surface of the layer farthest from the substrate and columnar crystals near the middle and bottom near the substrate. At a scan speed of 16 mm/s, the maximum angle between the scan speed and grain growth direction was 84 degrees. As the scan speed increased from 4 mm/s to 16 mm/s, crystal spacing decreased gradually from 13.3 to 9.2 microns in the columnar crystals.

A comparison of microstructure and mechanical properties between 316L SS produced through casting, hot-isostatic pressing (HIP) densification, selective laser melting (SLM), and a combination of SLM and HIP densification was performed by Röttger et al. [4]. Figure 6 shows an EBSD orientation diagram for these samples (a being the cast sample, b being the HIP-densified sample, c being the SLM-densified sample, and d being the combined SLM and HIP densified sample), while Figure 7 shows the yield strength, tensile strength, and elongation to fracture

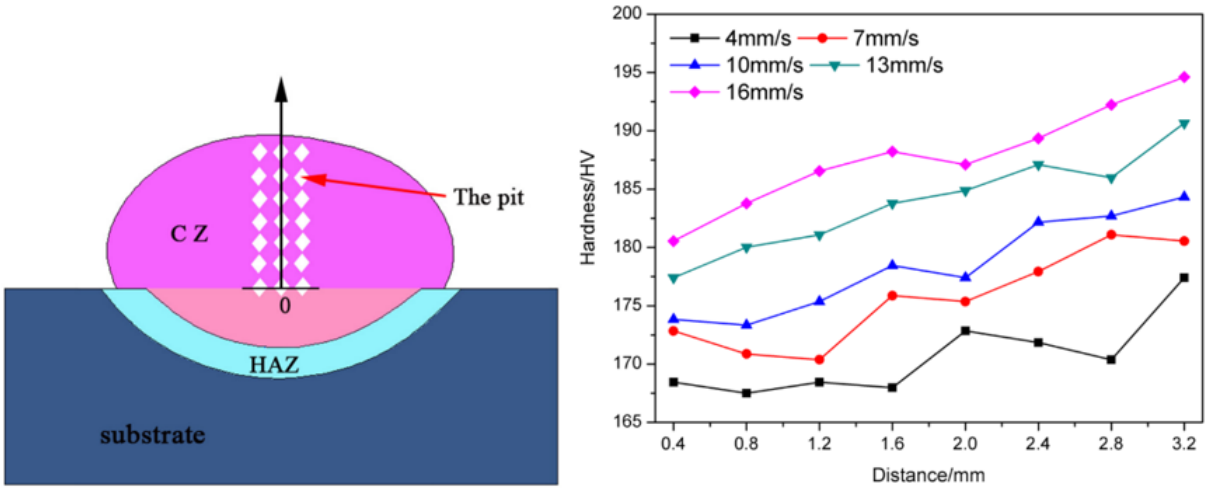

Figure 4: Left: diagram of cladding zone (CZ) used in hardness study. Right: microhardness of CZ versus distance along the axis on the left due to different scanning speeds [3].

values for various samples. The cast and HIP-densified samples were shown to have a dense microstructure, and the HIP postprocessing (for the HIP-densified and SLM+HIP-densified samples) causes the grains to become coarser and nearly equi-axial as shown in the top-right and bottom-right portions of Figure 6. Looking at Figure 7, SLM samples demonstrated superior yield strength compared to the case samples; this increased yield strength of the SLM samples was found to be due to their much smaller grain size as compared to those of the cast and HIP-densified samples with values of 25 versus 39 and 266 microns, respectively. However, the SLM samples showed a decreased elongation to fracture and Young's modulus as compared with the cast samples, decreasing from 200 GPa to approximately 144-166 GPa, respectively. The reason for this change was the increase in pores and cracking in the SLM-densified microstructure as compared to the other methods of fabrication. These results also showed that manufacturing 316L SS in the horizontal rather than in the vertical direction resulted in an increase in yield and tensile strengths of the samples.

In comparison to other processes, it's been confirmed in other studies that AM processes such as SLM can increase strength and ductility in stainless steels, including 316L SS [24] [25], with a study by Zhang et al. [26] producing samples with up to 657 MPa in tensile strength and microhardness up to 246 HV by using a flat placement and optimizing the hatch scanning to 30 degrees. This is particularly important for 316L SS as they have coarser grains which result in a deficient tensile strength than what is desirable for some industrial applications.

However, defects as a result of AM processes do occur. It introduces voids to the sample and results in different grain structures as compared to cast parts. Defects that are common to many AM processes include lack of fusion due to insufficient energy input/inappropriate scanning parameters, excessive energy leading to keyholing, and excessive scanning velocity leading to

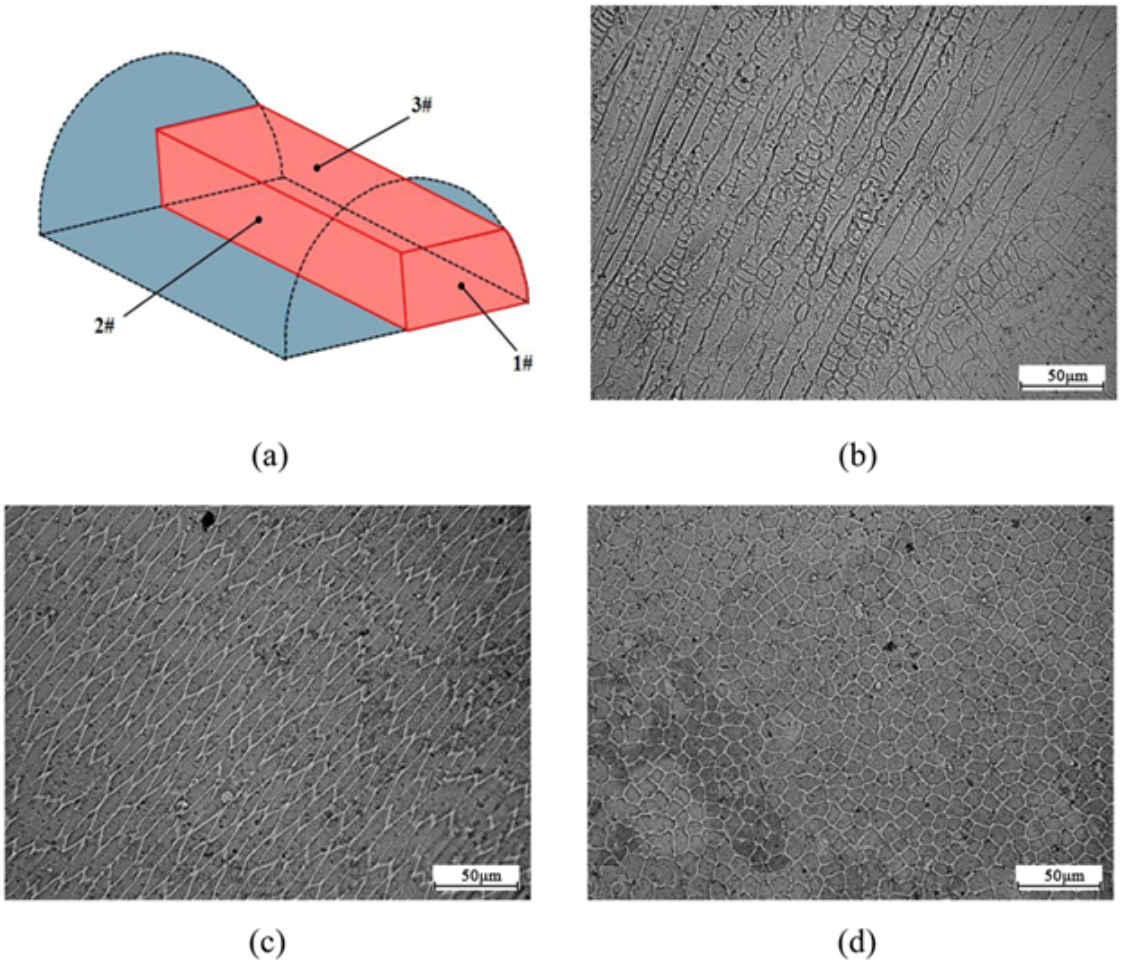

Figure 5: Microstructure of single-pass cladding layer: (a) diagram, (b) observation surface 1, (c) observation surface 2, (d) observation surface 3 [3].

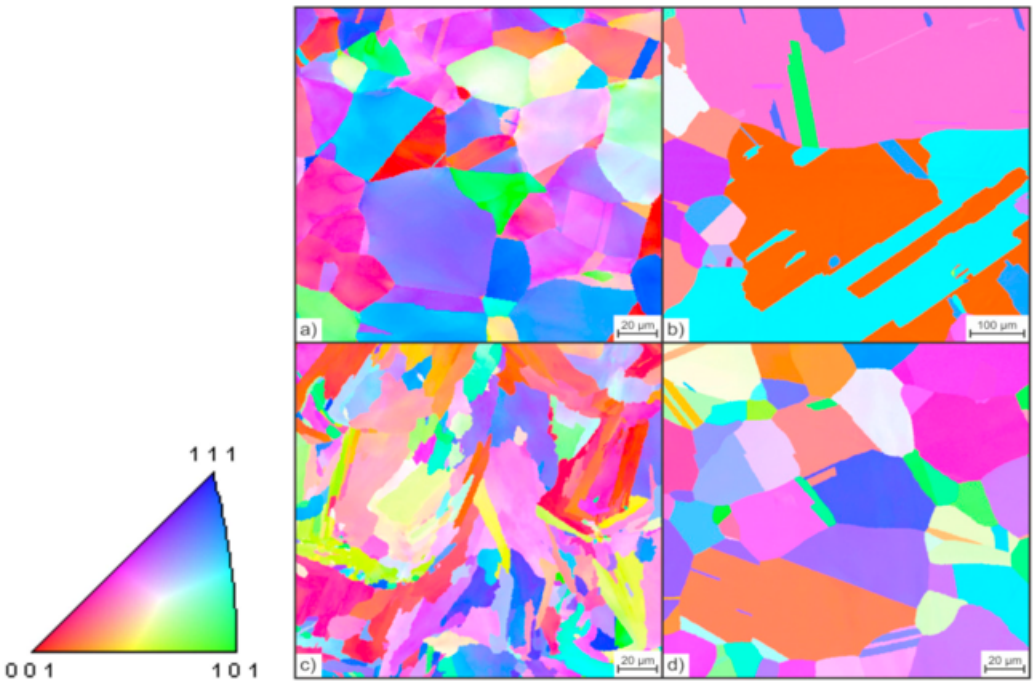

Figure 6: EBSD diagram for 316L SS samples. Left: orientation triangle. Right: EBSD orientations for a) cast, b) HIP-densified, c) SLM-densified, d) SLM+HIP-densified samples [4].

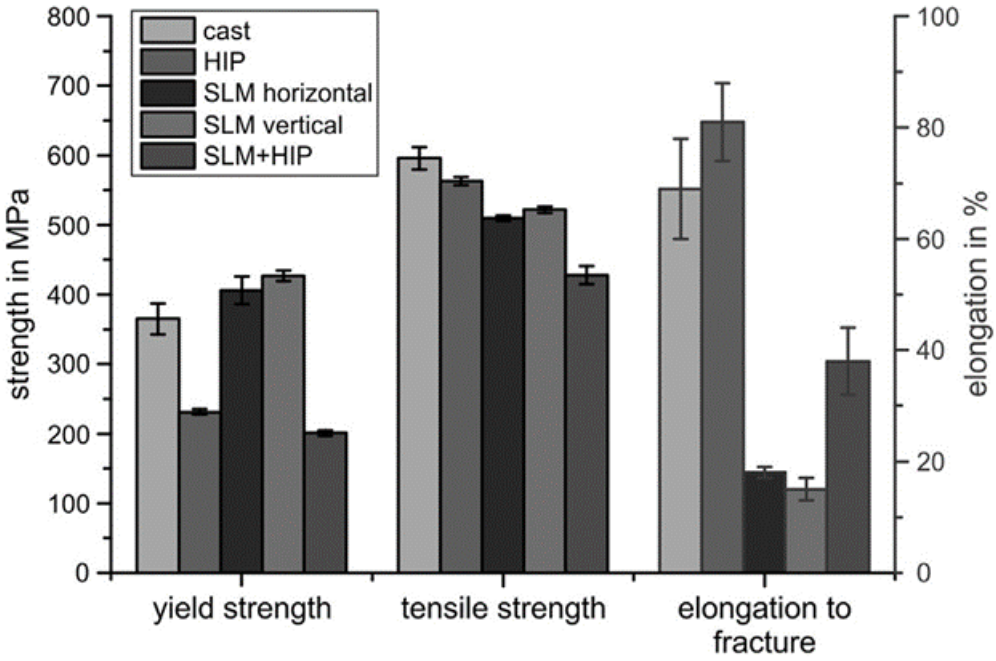

Figure 7: Material properties as a function of processing: cast, HIP-densified, SLM-densified in the horizontal direction, SLM-densified in the vertical direction, SLM+HIP-densified samples [4].

balling effects [27]. Generally, additively manufactured metal parts are considered inferior to cast parts due to problems with porosity and incomplete densification. The increased porosity and voids reduce ductility and increase the chances of stress ruptures as described by Sadowski et al.'s study of PBF processes on Inconel 718 [28]. This is not always the case, as a study by Rickenbacher et al. [29] of the nickel alloy Inconel 738 produced using AM demonstrated superior tensile strength to similar cast parts. Other issues with AM parts include thermal stresses and delamination of consecutive layers due to high thermal gradients and rapid thermal cycling as a part of the AM processes, as described by Chlebus et al. [30] and Simchi [1]. Promoppatum et al. [5] studied micro and macro characteristics of Ti-6Al-4V. A processing window was developed based on previous experimental data to prevent excess heating leading to over melting and insufficient heating leading to incomplete melting. In their study, measurements for roughness and hardness were made which demonstrated that the roughness and hardness increase as a function of energy density, though hardness leveled off after the 49.1 J/mm^3 energy density measurement. Figure 8 shows the microstructure of the top and side surfaces of the samples made with various powers and scanning velocity of 1357 mm/s. With the increasing energy density going from the top of the figure to the bottom, it's easily shown that the top layer of images showed balling and insufficient densification due to the lower energy density which is remedied at higher energy densities. In this same study, Promoppatum et al. [5] performed optical microscopy of Ti-6Al-4V sample exposed to single laser scanning lines on the titanium alloy powder at varying laser power levels. Figure 9 shows the results of these examinations. The left column of images in the figure which represents the results for the 50 to 150 W laser power range showed insufficient laser power to achieve consistent powder fusion. The right column of images in the figure where 150 W to 400 W of laser power was used shows powder fusion was consistently achieved in all three cases.

2.3 Summary and outlook

As this review has demonstrated, additive manufacturing has shown to have promising results in increasing the tensile strength of material samples as compared to cast samples, and allows for the fabrication of parts with varying density, form factor, and porosity. As the topic continues to be studied, more experimental and modeling work will need to be done, particularly for predicting process parameter effect on structure and material properties and evaluating the performance of the AM materials in nuclear environments.

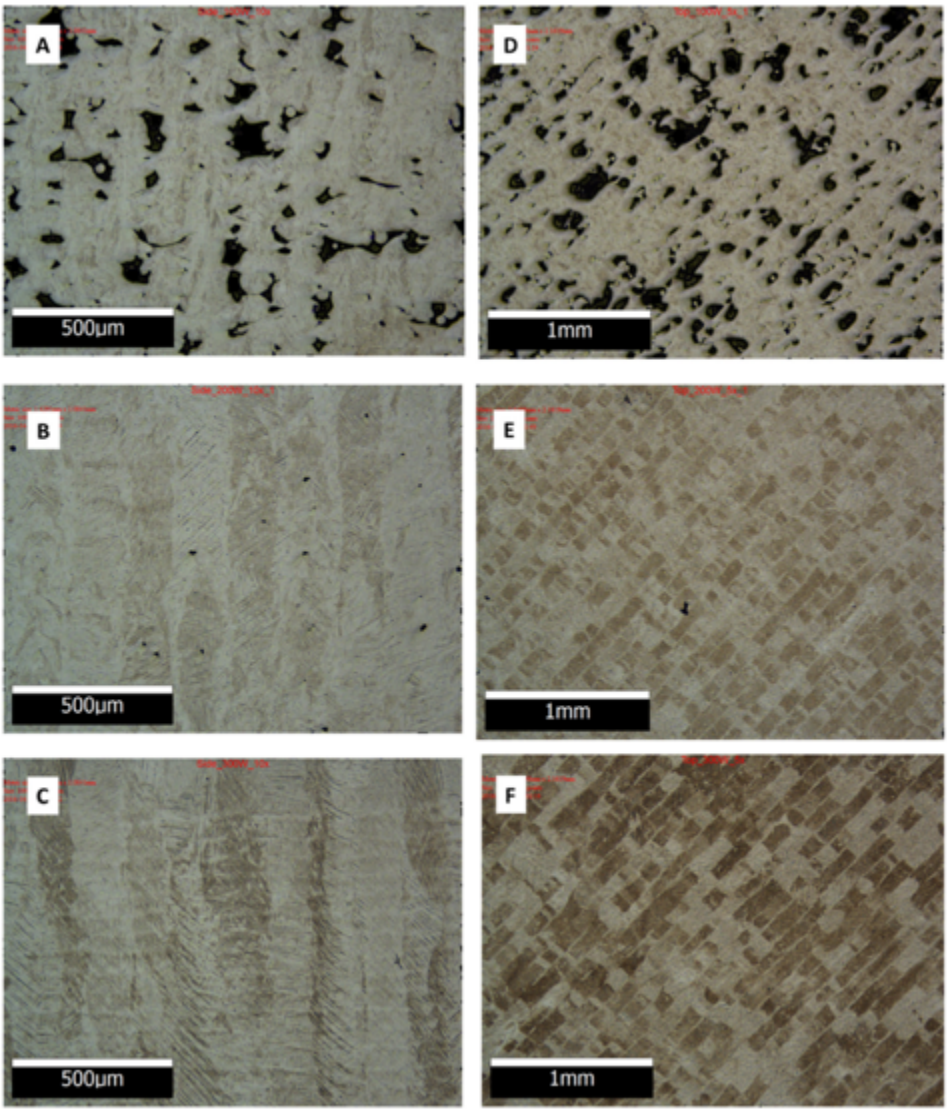

Figure 8: Microstructure of the top and side surfaces of the samples studied by Promoppatum et al. [5]. The energy densities vary as follows in units of J/mm3 and by location: a) 24.6, side surface; b) 49.1, side surface, c) 73.7, side surface, d) 24.6, top surface, e) 49.1, top surface, f) 73.7, top surface.

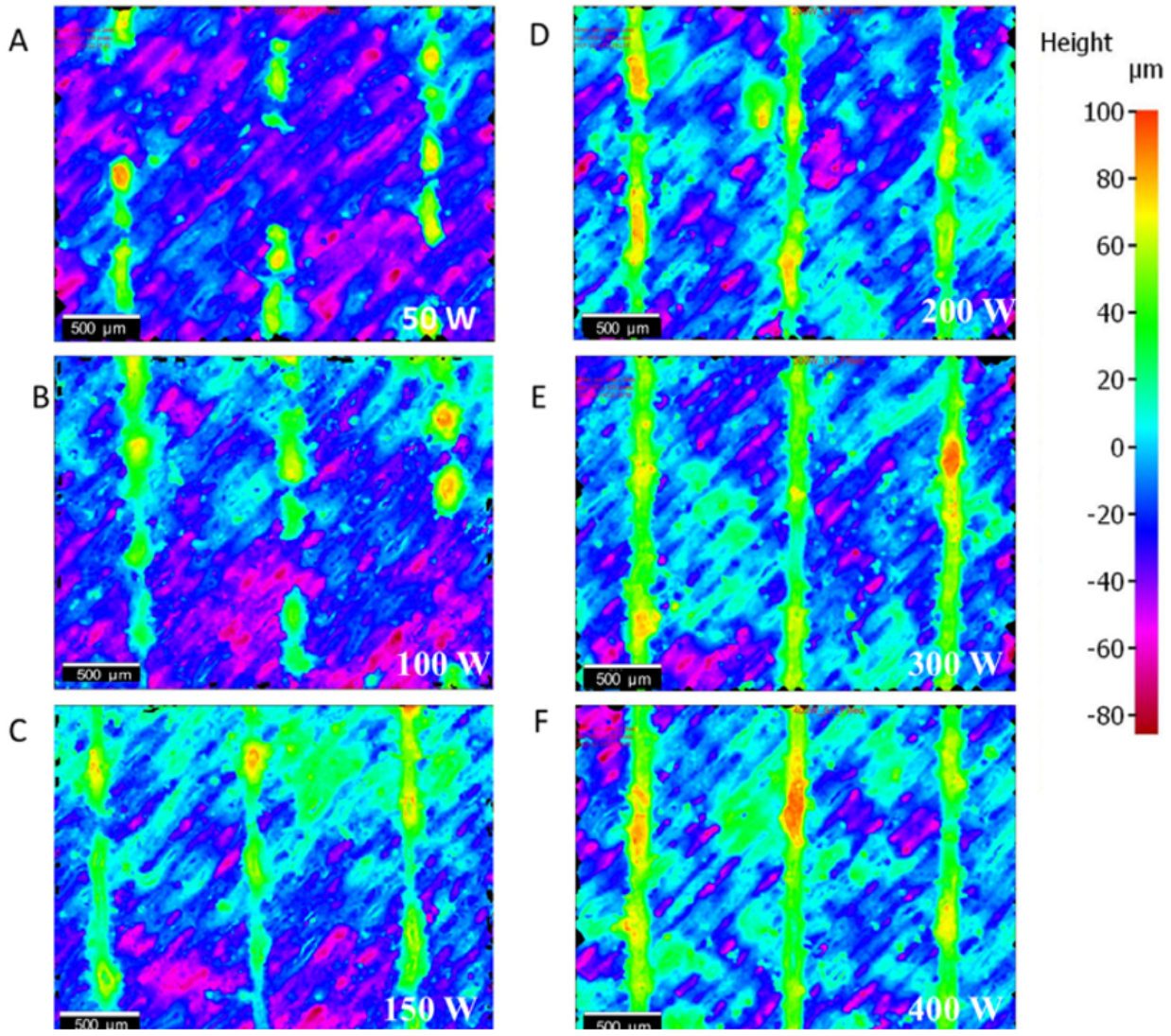

Figure 9: Surface contours of single scanning lines at a fixed velocity of 1357 mm/s for varying laser powers as studied by Promoppatum et al. [5].

3. Physics-based Models

Laser powder bed fusion (LPBF) technique is a complex process involving melting of powder particles and eventual solidification to form a complex grain structure. During the process, the substrate and prior build layers absorb energy and form a local melt pool via phase change, where powder is continuously added and melted to build up the next layer. The rapid cooling rate causes changes in the microstructure and the layer-wise manufacturing causes anisotropy in the build direction, thus changing the mechanical properties with respect to wrought material. Hence, understanding the LPBF process and its impact on the microstructural evolution of the material necessitates development of a multiscale multiphysics models, models that capture and correlate the intricacies of the AM process and the corresponding microstructure formation. The inter connection between different physics-based models is shown in Figure 10.

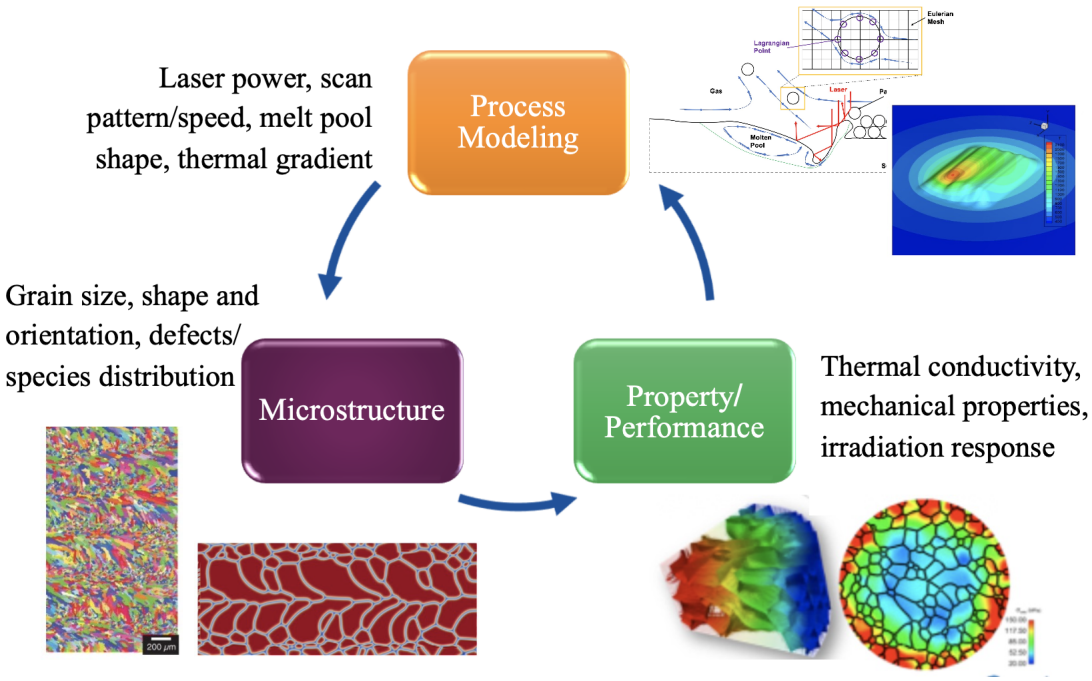

Figure 10: Schematic of the multiscale modeling components for establishing the PSPP correlation for AM

3.1 AM Process Models

This section focuses on development of a fluid-thermal models for the LPBF technique to predict the melt pool dynamics. The formation of a melt pool is a nonlinear, non-equilibrium multiphysics process resulting in a large thermal gradient, high cooling rates, and high solidification front velocities. Understanding the melt pool dynamics is an important intermediate step to correlate how the process conditions influence the microstruture of the final product. Temperature histories obtained from the melt pool simulations can serve as an input to the

microstructural evolution model to capture the solidification and grain formation from the powder materials during the process. Computational fluid dynamics (CFD) models are widely used to simulate the melt pool dynamics at the continuum scale. In , two methods, i.e., the level-set method and the Arbitrary Lagrangian-Eulerian (ALE) method, are used to track the moving melt pool boundaries. In this section we present the improvements made to the existing models in MALAMUTE to enhance it's the process modeling capabilities.

3.1.1 Level Set Model

In MOOSE Application Library for Advanced Manufacturing UTilitiEs (MALAMUTE), a set of fully coupled equations are solved for the melt pool dynamics using a Newton's approach. They include the level set equation [6],

$$\frac{\partial \phi(\vec{x},t)}{\partial t} + \vec{u}(\vec{x},t)\cdot\nabla\phi(\vec{x},t) + F_p|\nabla\phi(\vec{x},t)| = 0\,, \tag{8}$$

the mass conservation equation,

$$\nabla\cdot\vec{u}(\vec{x},t) = 0\,, \tag{9}$$

the energy conservation equation,

$$\rho\frac{\partial h}{\partial t} + \rho\nabla\cdot(\vec{u}h) = \nabla\cdot(k\nabla T) + \frac{2P\alpha}{\pi R_b^2}\exp\left(\frac{-2r^2}{R_b^2}\right)|\nabla\phi| - A_h(T-T_0)|\nabla\phi| - \sigma\varepsilon(T^4-T_0^4)|\nabla\phi|\,, \tag{10}$$

and the momentum equation,

$$\rho\left(\frac{\partial\vec{u}}{\partial t} + \vec{u}\cdot\nabla\vec{u}\right) = \nabla\left[-p\mathbf{I} + \mu\left(\nabla\vec{u} + \nabla\vec{u}^T\right)\right] - \rho_l\beta_l(T-T_r)\vec{g} - \frac{\mu_m}{K}\vec{u} + \gamma_T\nabla_s T|\nabla\phi|\,. \tag{11}$$

The symbols used in the above set of equations are explained in Table 1.

Table 1: Notations for the melt pool simulations.

Parameters	Unit	Symbol
Level set function	m	$\phi(\vec{x}, t)$
Fluid velocity	m/s	$\vec{u}(\vec{x}, t)$
Powder addition speed	m/s	F_p
Density	$\mathrm{kg/m^3}$	ρ
Enthalpy	J/(kg)	h
Thermal conductivity	$\mathrm{J/(m \cdot s \cdot K)}$	k
Dynamic viscosity	$\mathrm{kg/(m \cdot s)}$	μ
Laser power	J/s	P
Effective beam radius	m	R_b
Laser energy absorption coefficient	–	α
Heat transfer coefficient	$\mathrm{J/(s \cdot m^2 \cdot K)}$	A_h
Stefan–Boltzmann constant	$\mathrm{J/\left(s \cdot m^2 \cdot K^4\right)}$	σ
Material emissivity	–	ϵ
Melt pool temperature	K	T
Ambient temperature	K	T_0
Thermal expansion coefficient	–	β_l
Gravity vector	$\mathrm{m/s^2}$	$\vec{g}$
Reference temperature	K	T_r
Isotropic permeability	$\mathrm{m^2}$	K
Surface tension coefficient	N/m	γ
Surface curvature	$\mathrm{m^{-1}}$	κ
Normal vector to the free surface	–	$\vec{n}$
Thermal capillary coefficient	$\mathrm{N/(m \cdot K)}$	γ_T

Figure 11 presents the powder deposition profile and melt pool dynamics modeled using the level-set approach in MALAMUTE.

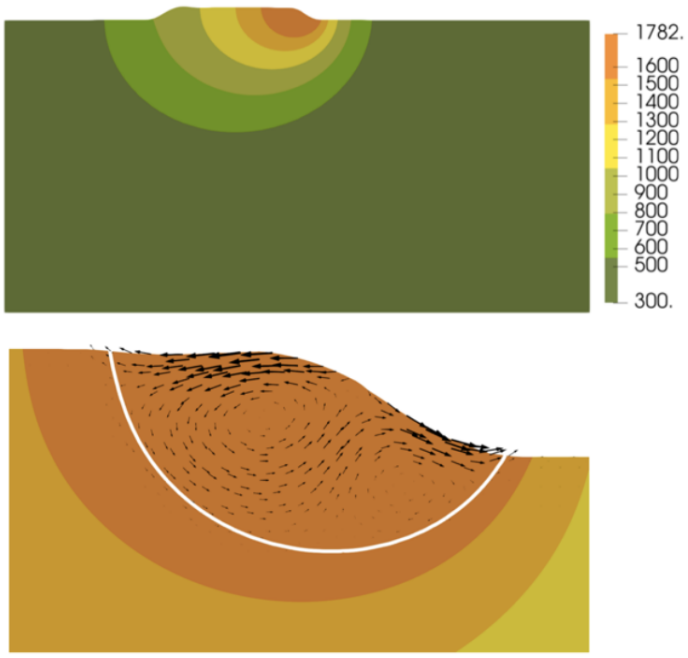

Figure 11: Modeling powder deposition profile (top) and fluid flow in the melt pool (bottom) using the level-set approach in MALAMUTE [6]

3.1.2 ALE Model

Aspects of laser melt pools such as pool motion and thermal distribution, may be modeled using Arbitrary Lagrangian Eulerian (ALE) techniques. The mass, energy, and momentum conservation equations are similar to Eqs. 9, 10, and 11, respectively, with the terms involving the level set variable ϕ removed. The advecting velocity $\vec{u}$ (in an Eulerian context the advecting velocity is just the material velocity) is modified to take the rate of mesh displacements into account: $\vec{u} \mapsto \vec{u} - \vec{u}_g$, where $\vec{u}_g = \partial\vec{d}/\partial t$ and $\vec{d}$ are the mesh displacements, e.g. how far points in the meshed simulation domain have moved from their initial configuration. In other words the advecting velocity in an ALE simulation is the material velocity minus the mesh velocity. In the results shown in this section, the heating from the laser source and radiative losses are modeled using surface terms as opposed to the volumetric terms shown in Eq. 10. Displacement of the melt pool surface can occur due to recoil from material evaporation, surface tension effects, and internal melt pool motion due to natural convection.

Finite element-based ALE modeling in Multiphysics Object-Oriented Simulation Environment (MOOSE) was first reported in Ref. [6]. The results in that work were generated using forks of MOOSE and the Portable Extensible Toolkit for Scientific Computation (PETSc) [31] that were not included in the main MOOSE repository. Input files that used syntax from the MOOSE fork and added solver robustness from the PETSc fork were checked into MALAMUTE, but could not be run since MALAMUTE uses the main MOOSE repository. In the past fiscal year we merged the MOOSE framework, heat conduction, and Navier-Stokes module enhancements from the forked

version into the main MOOSE repository such that any user can now reproduce the ALE results published in [6]. We demonstrate this new user capability in Fig. 12, in which a laser is rotated 360 degrees around a steel surface until it begins to ablate and displace condensed matter material.

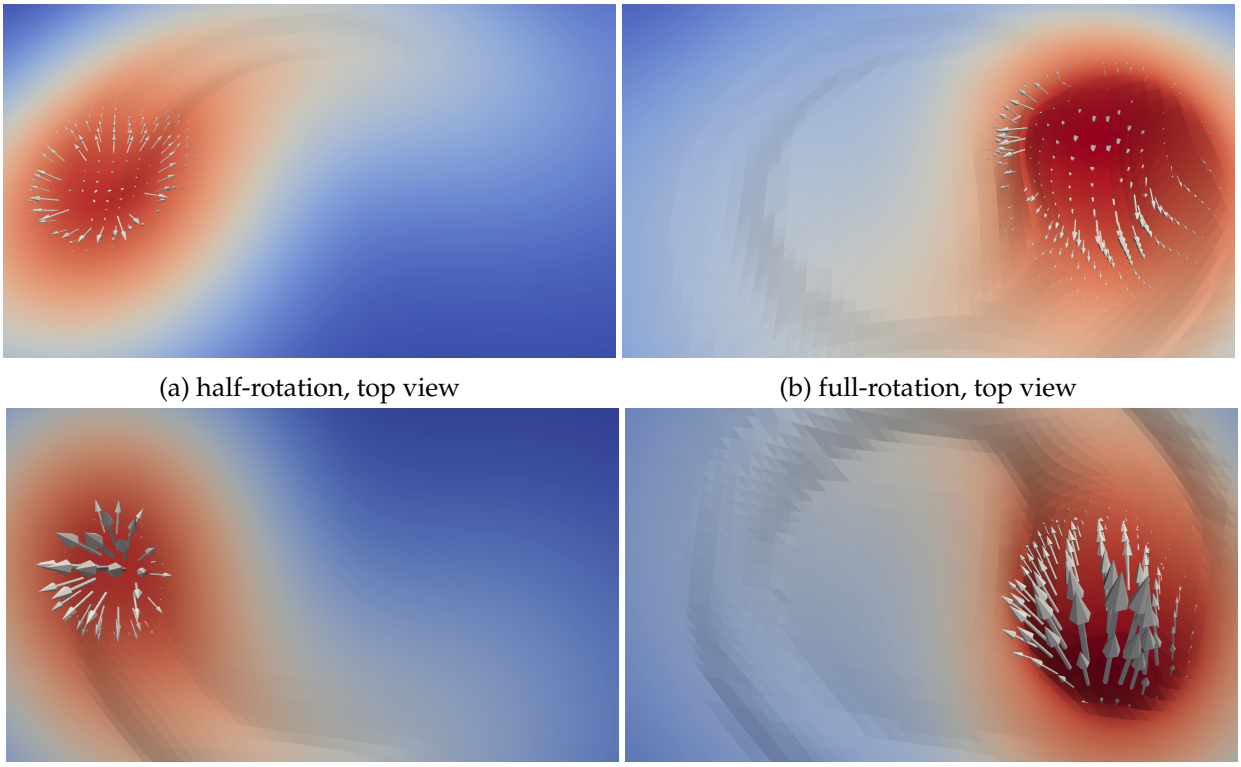

(a) half-rotation, top view

(b) full-rotation, top view

(c) half-rotation, bottom view

(d) full-rotation, bottom view

Figure 12: Visualization of just the top surface of the melt pool after a half and full rotation of the laser. Solid coloring is based on the temperature ranging from 300 K (dark blue) at the bottom of the domain (not shown here) to 3200 K (dark red) at the center of the laser spot. Arrow vectors are based on the material velocity vector. Arrow lengths are based on the velocity magnitude and are scaled 10 × larger for viewing purposes for the half-rotation compared to the full rotation.

In addition to moving finite element ALE capability into the main MOOSE repository, we spent the last fiscal year developing a coupled finite volume-finite element methodology for ALE simulations. The finite volume method has been added within the past three years to MOOSE. Its capabilities for modeling fluid flow are outlined in Ref. [32]. In the mixed finite volume-finite element scheme, pressure, velocity, and temperature variables and the associated mass, momentum, and energy equations respectively are discretized using a second order accurate finite volume method while mesh displacement variables are discretized using a continuous finite element formulation. We pursue the finite volume scheme for the conservation equations due to its local element-level conservation property, ability to handle discontinuous boundary conditions, and lack of complex stabilization schemes such as Streamline-Upwind Petrov-Galerkin. We keep the continuous finite element scheme for the displacement variables since the degrees of freedom are associated with nodes, allowing for a one-to-one mapping from

the displacement solution vector to displacement of the mesh nodes. Implementing mixed finite volume-finite element ALE required substantial changes to MOOSE. These included

- adapting MOOSE's finite volume implementation to be able to run on displaced meshes,
- defining evaluations for finite volume variables at nodes, which is where the mesh displacement degrees of freedom are located, and
- defining evaluations of finite element variables at face centers, which is where finite volume fluxes are evaluated.

Figure 13 illustrates the coupled finite volume-finite element methodology for a two dimensional simulation in which the laser is rastered back and forth in the middle of the domain. This is representative of the laser movement in the LPBF processes. Coloring is based on the temperature. Arrows point in the direction of the material velocity vector and are scaled according to the velocity magnitude. For the last time point shown (t=300) the laser spot is in the left half of the domain. Interestingly, at this time step, the coldest point in the domain is in the center-right. We can attribute this to the combined effects of surface radiative losses and the fact that heat is being convected away from the surface through bulk convection in the melt pool. The ability to couple these disparate discretizations on physics as intricate as ALE represents a great step forward in MOOSE and MALAMUTE capability. Moreover, this capability enable capturing the process variabilities with a physics-based computationally efficient model. Further verification and validation of the coupled finite volume-finite element results will be done in the future.

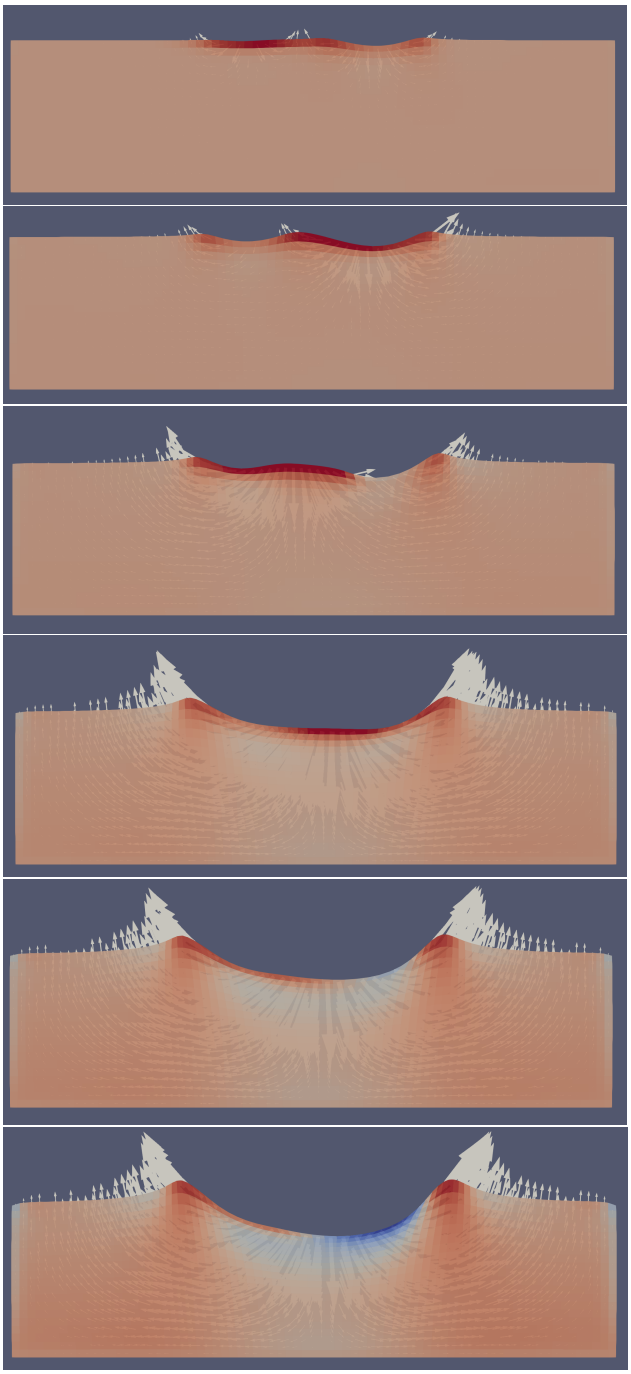

Figure 13: 2-D melt pool simulation using a mixed finite volume-finite element scheme. Arrows represent scaled velocity vectors. Solid coloring is based on the temperature. Times in arbitrary units are: 100, 150, 200, 250, 275, and 300.

3.2 Microstructural Evolution Model

To correlate the process conditions to the microstructural evolution, a multiphase phase-field model for epitaxial grain growth due to the solidification of 316 SS is developed in connection with the process conditions. There are two primary methods available in the literature for simulating the grain structure formation during the metal AM process: the cellular automaton (CA) method and the kinetic Monte Carlo (KMC) method. Both approaches predict the grain evolution as a voxel based on the thermal profile input and are therefore limited in terms of the underlying physics they can capture. However, the phase-field modeling (PFM) approach captures a physics-informed microstructural evolution and can be applied to predict the grain structure formation during the powder bed fusion process. Recently, a MOOSE-based polycrystal alloy solidification model has been developed that can predict the geometry of solidified structures based on the variation in thermal gradient and cooling rate [33]. Here, we extend the model to connect it to melt pool dynamics. To simplify the computational efforts, the microstructural evolution model is developed as a stand-alone model using analytical Rosenthal equation which provides the melt pool geometry and corresponding temperature distribution. We plan to connect it to the process models described in Section 3.1 using the MOOSE-based MultiApp approach [34]. The model captures the solidification and epitaxial and competitive grain growth that follows. Considering the rapid solidification that occurs during the AM process, the phase- field model utilizes the CALculation of PHAse Diagrams (CALPHAD) method to obtain the phase diagrams and the thermodynamic properties for 316L SS [35, 36]. In this section, we present the model formulation and its extension to incorporate the moving heat source and 316L SS properties, along with verification and preliminary demonstration of grain growth under moving melt pool.

3.2.1 Model Formulation

In this section, we present the phase-field model to capture the solidification and associated epitaxial grain-growth during laser powder bed fusion method. Phase-field modeling is a well-established approach for capturing microstructural evolution in various extreme conditions. Here, we utilize a grand-potential-based multi-phase multi-order parameter model to capture the microstructure formation during additive manufacturing process. The model was initially developed and implemented in MOOSE to capture alloy solidification [37**?** , 38]. Here we extend the model to couple it with a moving heat source and capture the epitaxial growth behaviors. The model represents a microstructure consisting of solid and liquid phases with K possible chemical species. For the solid phase, there are N_s possible grain orientations such that the individual grains are represented by a set of non-conserved order parameters: $\vec{\eta}_s = (\eta_{s1}, \eta_{s2}, \ldots, \eta_{sN_s})$. Within grain i, $\eta_{si} = 1$ and all other order parameters are 0. The interface between grains i and j is represented by the smooth variation of order parameters η_{si} from 1 to 0, and η_{sj} from 0 to 1. Finally, the liquid phase is represented by a single order-parameter η_l. In addition to the phases and crystallographic orientations, the chemical composition of the material system is represented with the help of the number density of the chemical components. Here, the number density ρ of

each solute species at each position is tracked in the model.

The evolution of the order parameters (η_l, η_{si}) are represented by an Allen-Cahn equation derived from the grand potential functional such that

$$\frac{\partial \eta_l}{\partial t} = -L\frac{\delta \Omega}{\delta \eta_l} \tag{12}$$

$$\frac{\partial \eta_{si}}{\partial t} = -L\frac{\delta \Omega}{\delta \eta_{si}} \tag{13}$$

Here, L is the Allen-Cahn mobility, and Ω is the total grand potential functional of the system:

$$\Omega = \int_V \left(\omega_{bulk} + \omega_{grad} + \omega_{chem}\right) \mathrm{d}V\,, \tag{14}$$

where ω_{bulk} is the bulk free energy density term, ω_{grad} adds the gradient energy contribution, and ω_{chem} incorporates the appropriate grand potential densities for each phase such that:

$$\omega_{bulk} = m\left[\left(\frac{\eta_l^4}{4} - \frac{\eta_l^2}{2}\right) + \sum_{i=1}^{n_s}\left(\frac{\eta_{si}^4}{4} - \frac{\eta_{si}^2}{2}\right) + \left(\frac{\gamma_{ls}}{2}\eta_l^2\sum_i^{n_s}\eta_{si}^2 + \sum_i^{n_s}\sum_{i\neq j}^{n_s}\frac{\gamma_{sisj}}{2}\eta_{si}^2\eta_{sj}^2\right) + \frac{1}{4}\right]\,, \tag{15}$$

$$\omega_{grad} = \frac{\kappa}{2}\left(|\nabla\eta_l|^2 + \sum_{i=1}^{N_s}|\nabla\eta_{si}|^2\right)\,, \tag{16}$$

and

$$\omega_{chem} = h_s\omega_s + h_l\omega_l\,. \tag{17}$$

Here, s and l represent the solid and liquid phases, i and j are the indices for the grains, N_s is the total number of grains, m is the free energy barrier coefficient, and γ_{ls} and γ_{sisj} are a set of constants that enable adjustment of the interfacial energy between solid and liquid phases as well as between the i^{th} and j^{th} grains of the solid phase, respectively. κ is the gradient energy coefficient, ω_s and ω_l are the local grand potential densities for the solid and liquid phases, and h_s and h_l are the switching functions used to interpolate the grand potential densities between the phases defined as

$$h_s = \frac{\sum_{i=1}^{n_s}\eta_{si}^2}{\eta_l^2 + \sum_{i=1}^{n_s}\eta_{si}^2}, \tag{18}$$

and

$$h_l = \frac{\eta_l^2}{\eta_l^2 + \sum_{i=1}^{n_s}\eta_{si}^2}, \tag{19}$$

for the solid and liquid phases, respectively [**?**]. The grand potential density for the phase $\omega_{s/l}$ is given by

$$\omega_{s/l} = f_{s/l} - \rho_A\mu_A - \rho_B\mu_B - \ldots - \rho_{K-1}\mu_{K-1}, \tag{20}$$

where $f_{s/l}$ is the Helmholtz free energy density of the phase considered and μ_A is the chemical potential between species A and the solvent.

The evolution equation is expressed in a generic form such that

$$\begin{aligned}\frac{\partial \eta_{\alpha i}}{\partial t} &= -L\frac{\delta \Omega}{\delta \eta_{\alpha i}} \\ &= -L\Bigg[m\left(\eta_{\alpha i}^3 - \eta_{\alpha i} + 2\eta_{\alpha i}\sum_{\beta=1}^{N}\sum_{j=1,\alpha i\neq\beta j}^{n_\beta}\gamma_{\alpha i\beta j}\eta_{\beta j}^2\right) + \frac{1}{2}\frac{\partial \kappa}{\partial \eta_{\alpha i}}\sum_{\beta=1}^{N}\sum_{j=1}^{n_\beta}\left(\nabla\kappa_{\beta j}\right)^2 \\ &\quad - \nabla\cdot\left(\frac{1}{2}\frac{\partial \kappa}{\partial \nabla\eta_{\alpha i}}\sum_{\beta=1}^{N}\sum_{j=1}^{n_\beta}\left(\nabla\kappa_{\beta j}\right)^2 + \kappa\nabla\eta_{\alpha i}\right) + \sum_{\beta=1}^{N}\frac{\partial h_\beta}{\partial \eta_{\alpha i}}\omega_\beta\Bigg].\end{aligned} \tag{21}$$

where, $\eta_{\alpha i}$ is the nonlinear variable that Equation 21 solves for, and $\eta_{\beta j}$ is the other coupled variables. αi and βj correspond to the different phases (solid and liquid) and the associated grains within the phases (for this problem, grains within the solid).

The evolution of the solute species is represented by the generalized diffusion equation,

$$\frac{\partial \rho_A}{\partial t} = \nabla\cdot\sum_{I=1}^{K-1} M_{AI}\nabla\mu_I, \tag{22}$$

where M_{AI} is a mobility coefficient. For the grand-potential-based model, however, the chemical potential of each species is used as a field variable for simulating the system [37]. Hence, the evolution equation is represented as

$$\chi_{AA}\frac{\partial \mu_A}{\partial t} = \nabla\cdot\left(M_{AA}\nabla\mu_A\right) - \sum_{\alpha=1}^{N}\sum_{i=1}^{n_\alpha}\frac{\partial \rho_A}{\partial \eta_{\alpha i}}\frac{\partial \eta_{\alpha i}}{\partial t}, \tag{23}$$

where χ_{AA} is the susceptibility. The derivation of Eq. 23 from Eq. 22 can be found in [38].

The free energy of the liquid is modified to incorporate the temperature effect, such that

$$\omega_s = \sum_{I=1}^{K-1} -\frac{1}{2}\frac{\mu_I^2}{V_a^2 k_I^s} - \frac{\mu_I}{V_a}c_I^{s,min}, \tag{24}$$

and

$$\omega_l = \sum_{I=1}^{K-1} -\frac{1}{2}\frac{\mu_I^2}{V_a^2 k_I^l} - \frac{\mu_I}{V_a}c_I^{l,min} - S(T - T_m). \tag{25}$$

Here, T_m is the melting temperature. The local temperature T at the steady state is prescribed using the analytical Rosenthal equation [39] described as

$$T(x,r) = T_0 + \frac{Q}{2\pi k_T r}\exp\left(\frac{-v}{2\alpha}(r+X)\right) \tag{26}$$

here T_0 is the ambient temperature, Q is the absorbed power from the heat source, k_T is the thermal conductivity, α is the thermal diffusivity, and v is the velocity of the hear source. r represents the radial position on the work piece from the heat source and calculated as $r = \sqrt{x^2+y^2+z}$, with x, y, z being the positional co-ordinates. The moving reference frame is related to the simulation

frame as $x = x - x_0 - vt$, $y = y$, and $z = z$. x_0 is the initial position of the heat source at $t = 0$. It is noteworthy that the temperature field moves with time. Although the ultimate goal is to connect the microstructural evolution model with the process model presented in Section 3.1 to connect the process parameters to the microstructural evolution, here we use the Rosenthal equation as a simplified starting points. It helps us capture the effect of moving heat source while keeping the modeling complexity and the computational cost low. For the initial condition we utilize the Rosenthal equation and define the liquid phase when $T \geq T_m$ and the solid phase when $T < T_m$. This results in a sharp solid/liquid interface. We use the following function to introduce a diffused interface, $\eta_l = 0.5 \tanh(\frac{T-T_m}{4}) + 0.5$. Within the solid phase we utilize the Voronoi tessellation algorithm to initialize the grain centers and assign multiple grains within the solid.

3.3 Incorporating 316L components

In this case, the material of interest is 316L stainless steel, which has three major components: Fe, Cr, and Ni. For simplicity, a binary Fe-Cr system is considered here. 316L stainless steel typically contains 18% to 20 % Cr. The phase diagram of the Fe-Cr system is presented in Figure 14a. A thermodynamic model based on Miettinen for the mixing parameters and Dinsdale [35] for pure component parameters are used to construct the Fe-Cr binary system with 11-wt% Ni for the Redlich-Kister model (RK) used by Miettinen [36]. It is noteworthy that solubility and diffusivity of Cr atoms in Fe varies greatly with temperature and Cr content. The Gibbs free energy of the system at different temperature is shown in Figure 14b. The grand potential density requires a one-to-one relationship between the composition and the chemical potential within a phase. As such, using the regular solution or RK thermodynamic model is not a viable option. An estimation can be made using a parabolic free energy density to model each phase, i.e. the double well at lower temperature is constructed with two parabolic free energies, one representing the Fe-rich phase and one representing the Cr-rich phase. An example of this fitting process is shown in Figure 14c, where the parabola is fitted to the Gibbs free energy with positive curvature. The fitting is performed for a temperature range of 300 K $\leq T \leq$ 1750 K to obtain temperature dependent k_i, c_i^{eq}, and f_i^{min} for both liquid and solid phases.

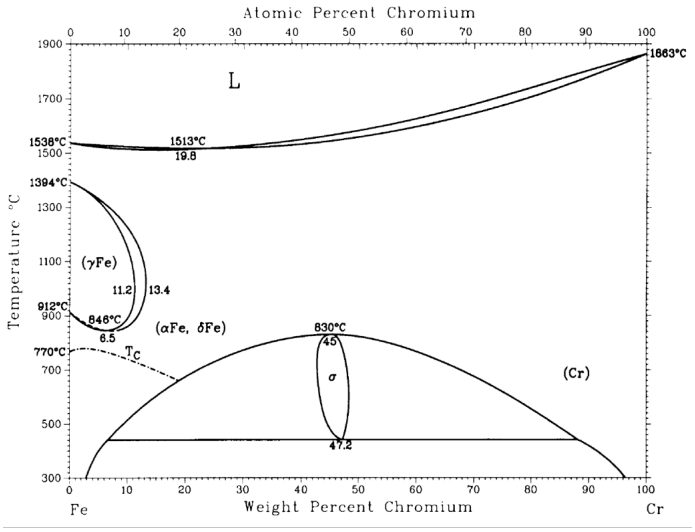

(a)

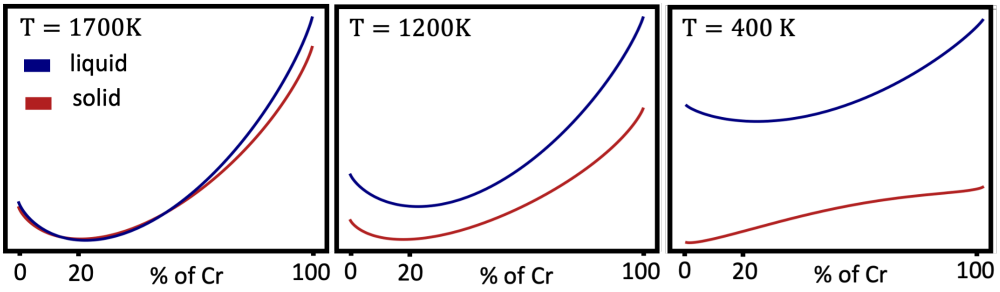

(b)

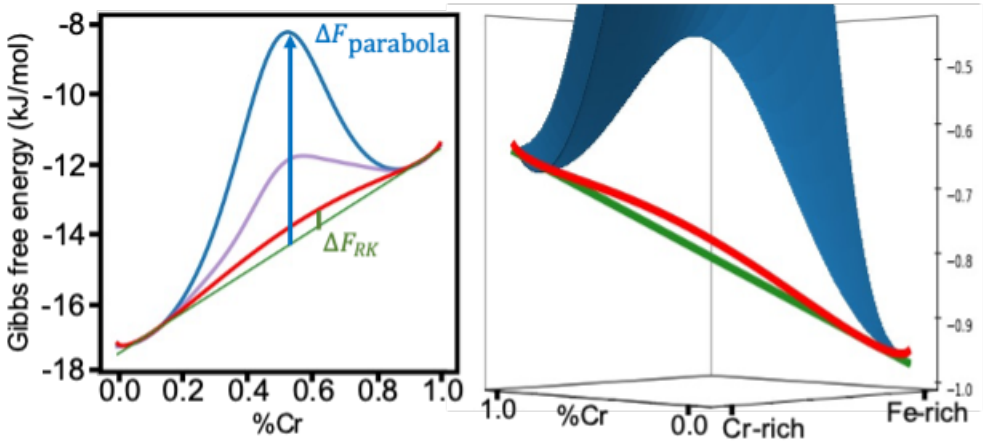

(c)

Figure 14: (a) Fe-Cr phase diagram (b) Gibbs free energy at different temperatures, c) parabolic fit.

3.3.1 Model Verification

Some initial tests are run for verification purposes. Two cases are considered, an isothermal spinodal decomposition at 500 K, and a phase segregation under a linear temperature gradient of

$(300K \leq T \leq 1600K)$. For each of the cases, the initial condition for the chemical potential (μ) is set up using a random seed between the value of 0.5 and 1.5. The order parameter values are slightly perturbed from their respective equilibrium values of 0 and 1. Parameter k_i and f_i^{min} are converted from J/mol to J/m^3 using the molar volume of pure Fe, and other energy density parameters are scaled with 1×10^7 J/m^3 energy scale and 1×10^{-6} m length scale. The diffusivity is set to a constant to speed up the microstructural evolution for testing purposes. The result from the first test shows a typical spinodal decomposition such that the Cr-rich phase nucleates and grow in a small region (see Figure 15). The perturbation of the order parameters facilitate the phase separation, leading to the spinodal decomposition. For the second case, the spinodal decomposition is less pronounced because the Cr-rich phase grows competitively across temperature and composition, see Figure 16. Despite higher Cr concentration at high temperature, the Cr-rich phase is thermodynamically less stable, thus it only appears at the lower temperature region. This is similar to what has been observed experimentally.

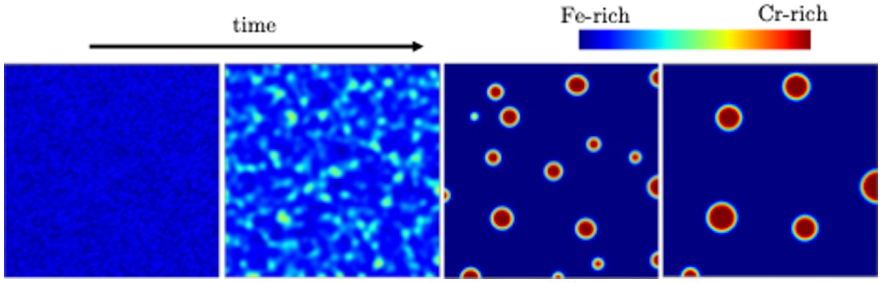

Figure 15: Spinodal decomposition of the Fe-rich and Cr-rich phases at 500 K temperature

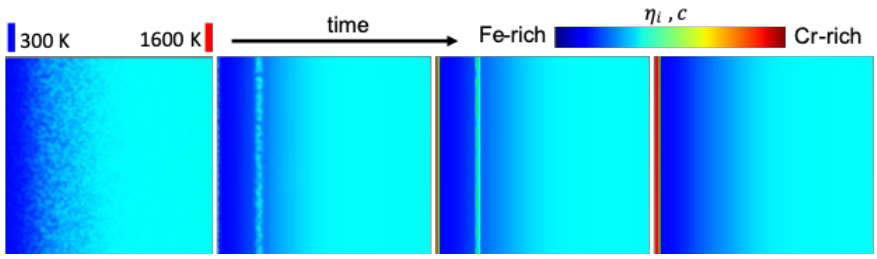

Figure 16: Chromium segregation under thermal gradient

3.3.2 Grain growth under a moving heat source

To understand the role of moving heat source on the grain evolution, we first look at the evolution of the grain boundary under the influence of a moving melt pool. The initial grain structure is designed such that the melt pool moves through the boundary of a bi-crystal structure. The temperature profile is initialized to follow the Rosenthal equation Eq. 26 and the chemical potential is initialized as a function of temperature. The interfacial width and gradient energy coefficients are kept constant. The liquid diffusivity is set to 0.15 and the solid diffusivity is

coupled with temperature through: $D_s = D_0 \exp(-Q/RT)$, where D_s is the solid diffusivity, $D_0 = 1.5 \times 10^{-5}$ m ^{2}/s is the diffusivity prefactor, $Q = 210,000$ J/mol is the activation energy, R is the gas constant, and T is the temperature field. Figure 17 shows the evolution of the GB under the influence of the moving melt pool and associated Cr segregation observed in the simulation. In this case, Cr accumulation occurs at the melting front such that the liquid becomes a Cr sink. A thin Cr segregation layer is observed at the liquid-solid interface is due to the temperature-dependent Cr solubility in the Fe-rich phase. The solidification front shows a reduction in the Cr content due to the lower Cr solubility in the Fe-rich phase at lower temperatures. The region near the left boundary shows lower Cr content due the moving melt pool absorbing Cr content and dragging it to the right. The Fe-rich phase appears to not fully solidify ($\eta_s < 1.0$) near the solidification front. Similar segregation behavior has also been observed experimentally. It is also observable is that the GB tends to always remain normal to the solid-liquid interface leading to change in the curvature of the GB. This also provides the reasoning of the dragging and rotation of the triple junction at the solidification front observed during AM processes which ultimately leads to formation of elongated grains.

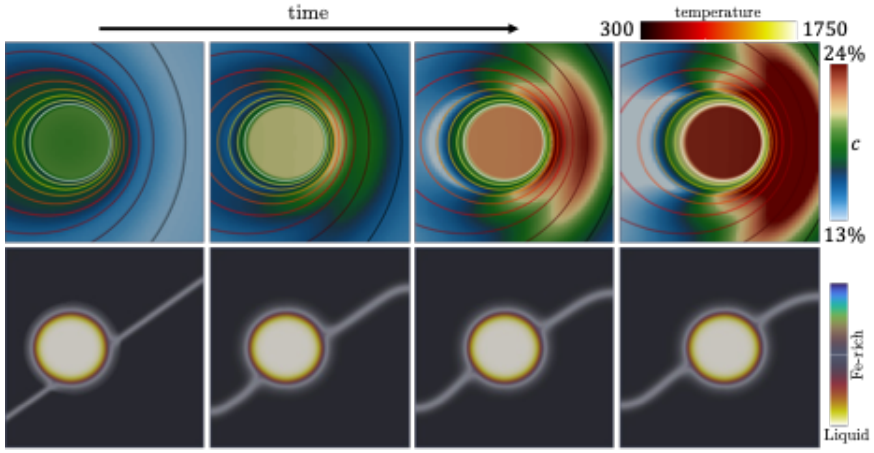

Figure 17: Evolution of the grain boundaries and Cr segregation under a moving heat source

Next, to test the model for a simple polycrystal structure, we simulate a small domain with 6 grains . The grain sizes and the initial melt pool size are selected such that the melt pool size is comparable to the grain size. Figure 18 depicts the time evolution of the microstructure. Similar to the previous case, the GB dragging effect and the rotation of triple junctions are observed in this case.

Finally, we consider a larger domain with 120 total grains and a melt pool much larger than the surrounding grains to simulate a realistic AM microstructure. The model captures realistic grain evolution leading to the formation of elongated grains. At the melting front, some grains are observed to be dragged with the melt pool without melting. It is not yet well understood whether this behavior is physical or not. This could be due to the diffused interface nature of the phase-field model. Since the solid-liquid interface does not reach the melting temperature, a

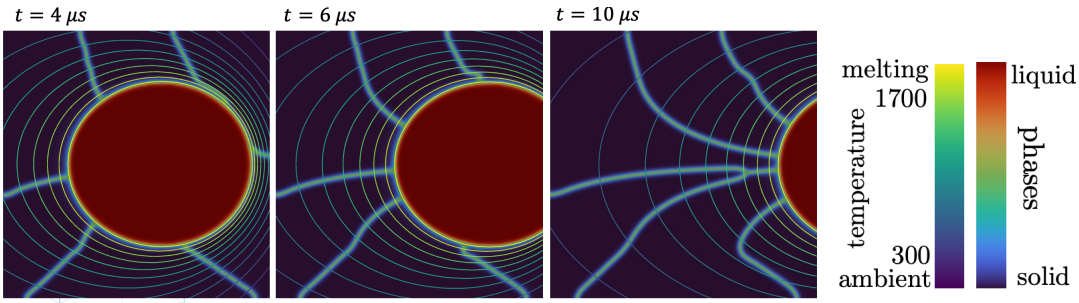

Figure 18: Epitaxial grain growth under moving heat source

complete transformation of the grains does not occur until the grains reach the interior of the melt pool. A penalty function needs to be designed to mitigate this issue. This will be addressed in the following fiscal year.

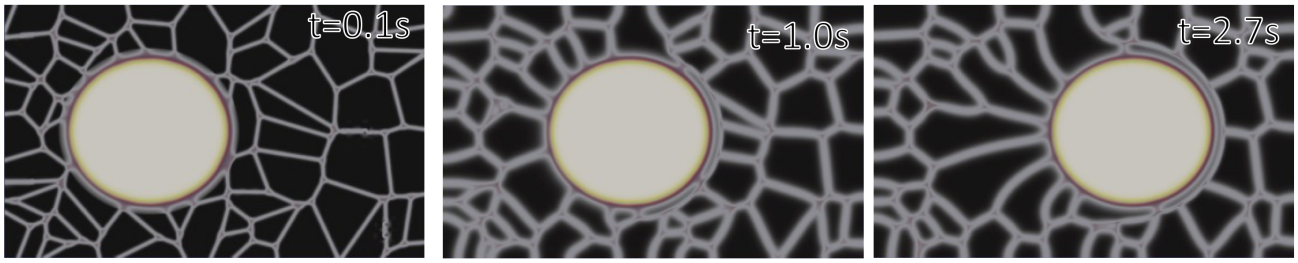

(a) (b) (c)

Figure 19: Epitaxial grain growth of a larger domain

4. Machine Learning Models

The numerical modeling of the AM process using MOOSE is a very expensive task especially considering that these models have to be run numerous times under varied or stochastic process conditions. To alleviate this large computational burden, we are using surrogate models that come with in-built prediction uncertainties. These prediction uncertainties will help us quantitatively assess when the surrogate predictions can be trusted and under what input conditions the surrogate needs to be re-trained in order to reduce its prediction uncertainty. Specifically, we are relying on the multi-output Gaussian processes (MOGPs) because they provide both mean predictions and associated uncertainties due to following a Bayesian formulation. In addition, MOGPs capture output covariances between field quantities like temperature and this improves their predictive performance compared to standard Gaussian processes given the same training data set. While these properties of MOGPs are attractive to accelerate the modeling of AM, MOGPs are expensive to train. Their training cost scales cubically with the number of outputs to predict. That is, if we want to predict a field quantity at 100 locations in the domain, the MOGP training cost is proportional to 100^3. To tackle this high computational burden, we are using dimensionality reduction methods to project the high-dimensional output space into a smaller dimensional latent space. It is in this latent space the MOGP will be trained and evaluated. The MOGP predictions in the latent space are transformed back into real space with an inverse map. This substantially reduces the MOGP training cost. For example, if the 100-dimensional output space is reduced to a 5-dimensional latent space, the MOGP training cost reduces to being proportional to 5^3 instead of 100^3. Moreover, both MOGPs and dimensionality reduction are being implemented in the MOOSE STM. The future vision for these capabilities is to accelerate the numerical computations of the AM process, while ensuring the robustness of the surrogate predictions by monitoring the prediction uncertainties, and couple them into an active learning framework where the surrogate and computational model interact with each other depending upon the input process conditions. A schematic of the ML framework in presented in Figure 20.

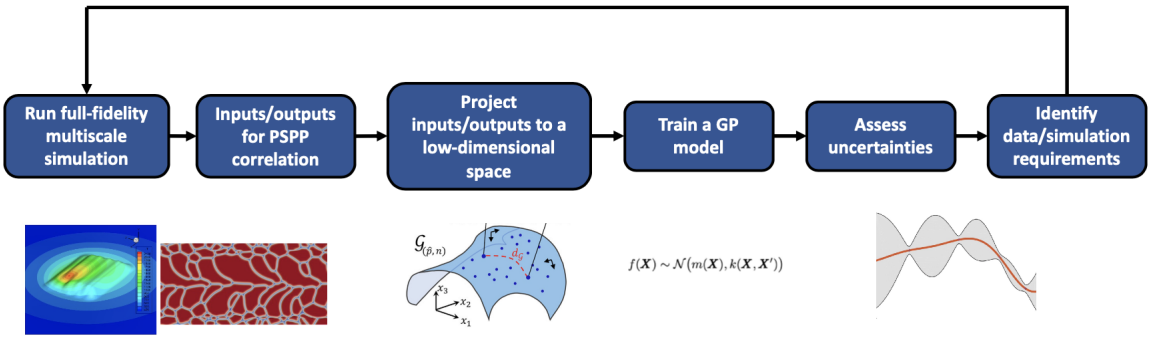

Figure 20: Schematic of the ML modeling framework

In this chapter, we will outline the initial developments pertaining to surrogate modeling using MOGPs and dimensionality reduction using PODs (or linear principal component analysis).

We outline the theory behind these techniques, test them on some benchmark case studies, and discuss their implementation in MOOSE STM.

4.1 Genetic Programming Based Symbolic Regression

In this section, we present a genetic programming based symbolic regression (GPSR) approach that was used to obtain the cooling rate as a function of laser speed and power. In general, symbolic regression (SR) is a type of regression analysis that searches the space of mathematical expressions to find the model that best fits a given dataset without assuming its form *a-priori*. It only assumes that the data can be fitted using some algebric expressions and then uses an algorithm to search for the correlation. GPSR is a type of SR that uses the genetic programming search algorithm to find the best fitting function for the data. This reduced order approach can quickly provide the cooling rate as a function of process parameters using the outputs from the physics-based process simulations. To generate the training data, we used a domain with the size of $x \in \{0, 0.015\,m\}$ and $y \in \{0, 0.015\,m\}$. The starting position of the laser is $x = 0.005\,m$, and $y = 0.005\,m$. The temperature distribution is measured at $x = 0.006\,m$, and $y = 0.0048\,m$. The temperature distribution is measured as the laser power is varied from 70 J/s to 100 J/s, and the laser velocity is varied from 0.004 m/s to 0.012 m/s. Figure 21 shows the temperature histories generated from the physics-based process simulations that are used to generate the training data set used by GPSR. Figure 22 presents the said training data sets. Total 440 data are generated through INL-HPC using stochastic tools of MOOSE [40]. Cooling rate is calculated from the temperature distribution data.

The hyper parameters setting for GPSR are listed in Table 2.

Table 2: Hyper parameters settings for GPSR

Hyper Parameters	Value
Operators	$\{+, -, \times, \div, \sin, \cos, \exp\}$
Complexity	23
Population	100
Maximum Iterations	1000
Tolerance	10^{-4}

The training evolution process is shown in Figure 23. The Pareto front plot (Fig. 23) explains the process to obtain the best symbolic equation fitted to the given data set. The fitness value is the numerical mean value of the 50 sampled symbolic equations, selected through permutation and combination of the operators. There are fluctuations because of the randomness. Overall, the trend of the graph increases from 0.65 to 0.92, and the level of fluctuations decreases in the end, which indicates that an optimal fitting expression is achieved.

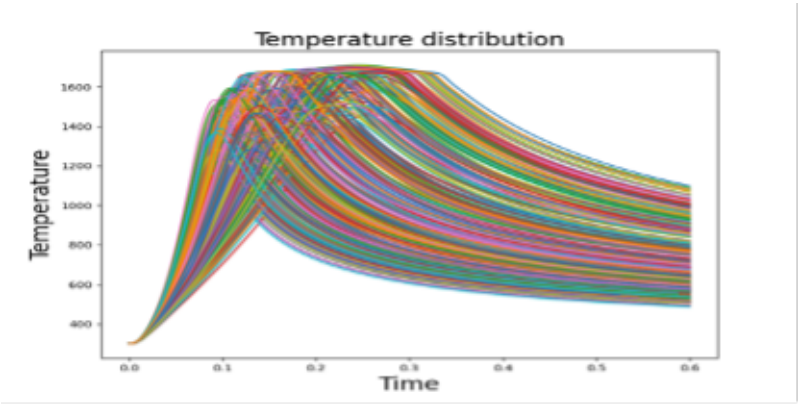

Figure 21: Temperature histories from the training data.

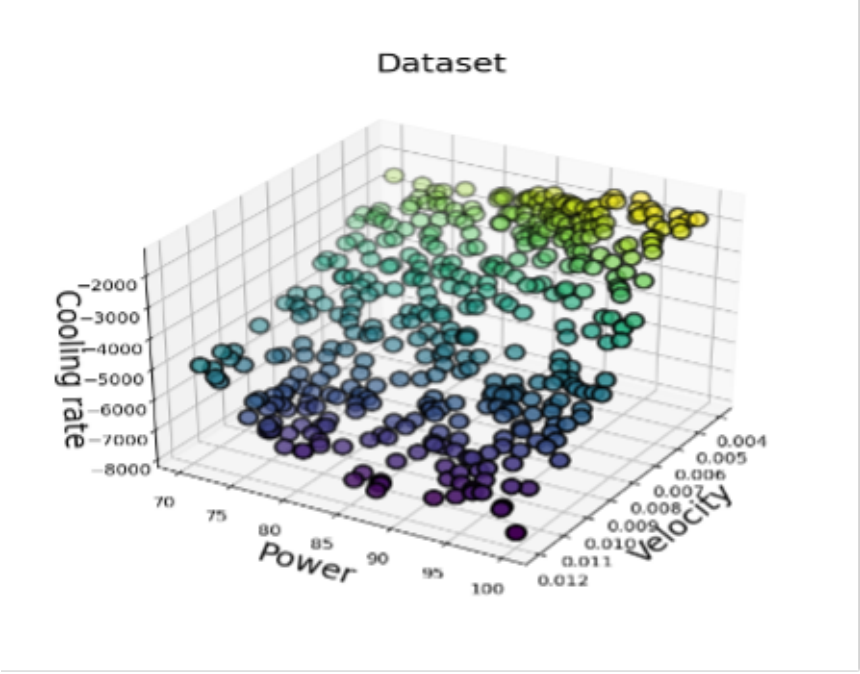

Figure 22: Training data obtained from the physics-based melt pool simulations.

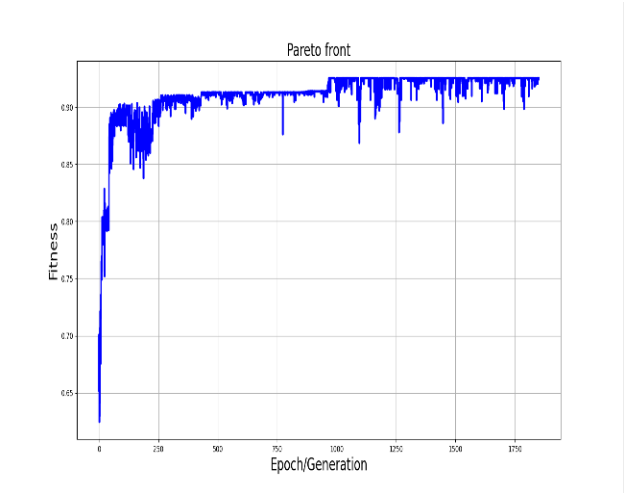

Figure 23: Pareto front plot (evolution process)

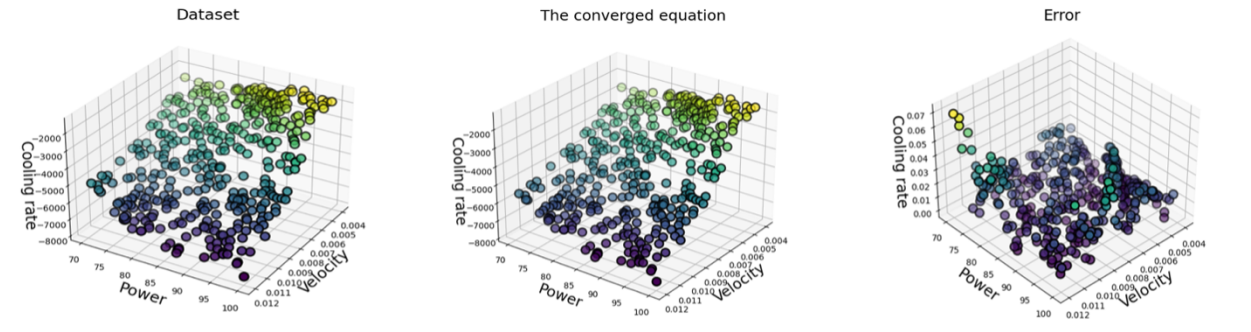

Figure 24: The error of the converged equation.

The converged equation is given as

$$f(v,p) = 7790.05\left(-v_n + \sin\left(-5.602 v_n \exp\left(-2p_n\right) + p_n + 1.428\right) + 1.003\right) \tag{27}$$

where $v_n = v/0.0119$ and $p_n = p/99.93$ Figure 24 compares the training data set with the predictions of the converged equation, along with the error estimations. The ROM obtained from this analysis has a 92.53% accuracy. This presents a simplified ROM that connects the process variability to the final cooling rate with reasonable accuracy. This ROM equation can be further used in the phase-field-based solidification simulation to capture the influence of the cooling rate on the final microstructure.

4.2 Proper Orthogonal Decomposition

To enable the generation of accurate Reduced-Order Models (ROMs) for field quantities, such as temperature and concentrations, many techniques utilize dimensionality reduction methods. The common feature of these methods is that they map the fields of interest into low-dimensional latent spaces where the parametric behavior of the fields can be more easily learned by the ROMs. For this reason, a Proper Orthogonal Decomposition (POD)-based [41, 42] dimensionality reduction technique has been added to MOOSE.

4.2.1 Theory

POD has been widely used for dimensionality reduction purposes across multiple scientific principles. Depending on the field, the same concept is often referred to as Principal Component Analysis (PCA) [43], Karhunen-Loéve [44] expansion or Singular Value Decomposition (SVD) [45] as well. The essence of the method is that a lower-dimensional space (latent space) is determined in a way that it is closest to the given data in a certain norm. In this work, we use a discrete L^2 norm which can be defined as

$$|\vec{v}|_2 = \sqrt{\vec{v} \cdot \vec{v}}\,, \tag{28}$$

where $\vec{v} \in \mathbb{R}^N$ is a high-dimensional vector (N is large). This vector can be obtained by carrying out a high-dimensional field measurement or by exercising a numerical model. Due to the nature of work presented here, we generate these high-dimensional vectors using numerical models of advanced manufacturing processes. The procedure of obtaining a latent subspace of reduced dimensionality for the fields (vectors) in our problem consists of multiple steps:

1. The output of the numerical models often changes through simulated time or with the substitution of different input parameters. To start, we survey the time and input parameter-dependent high-dimensional solution manifold by taking snapshots of the fields (vectors) of interest at different time-parameter combinations. These vectors can then be organized in a snapshot matrix:

$$\boldsymbol{S} = \left[\vec{s}_{\mu_1,t_1}\ \vec{s}_{\mu_1,t_2}\ \vec{s}_{\mu_1,t_3}\ ...\ \vec{s}_{\mu_1,t_{N_{T_{\mu_1}}}}\ \ \vec{s}_{\mu_2,t_1}\ \vec{s}_{\mu_2,t_2}\ ...\ \vec{s}_{\mu_{N_\mu},t_{N-1}}\ \vec{s}_{\mu_{N_\mu},t_{N_{T_{\mu_{N_\mu}}}}} \right] , \tag{29}$$

where N_μ is the number of different model parameter samples, $N_{T_{\mu_i}}$ is the number of snapshots per transient simulation with parameter sample μ_i, while $\boldsymbol{s}_{\mu_i,t_j}$ denotes the vector of interest corresponding to parameter sample μ_i at time step t_j. Note that the number of time steps might depend on the model parameters, therefore the total number of snapshots (N_s) is given by:

$$N_s = \sum_{i}^{\mu} N_{T_{\mu_i}}. \tag{30}$$

2. We assume that the number of snapshots is considerably smaller than the number of entries in the high-dimensional vector ($N_s << N$). As the next step, the common features are extracted from the snapshots. In a discrete case such as this work, POD and SVD are equivalent so we can obtain these features by computing the SVD of the snapshot matrix:

$$\boldsymbol{S} = \boldsymbol{U}\boldsymbol{\Sigma}\boldsymbol{V}^T \tag{31}$$

where $\boldsymbol{U}$ and $\boldsymbol{V}$ are the unitary left and right singular vector matrices, while matrix $\boldsymbol{\Sigma}$ contains the singular values on its diagonal. Throughout this work, due to their equivalence, left singular vectors will also be often referred to as POD modes. It can be shown [46] that the first r left singular vectors from $\boldsymbol{U}$ (first r columns) span an optimal basis which is closest to the snapshots in a discrete L^2 sense. Therefore, we can use these singular vectors to approximate our high-dimensional vector of interest as:

$$\vec{s} \approx \boldsymbol{U}_r \vec{c}_r\ , \tag{32}$$

where vector $\vec{c}_r \in \mathbb{R}^r$ contains the reduced-order coefficients or coordinates in the latent, low-dimensional space. Note that $\boldsymbol{U}_r$ contains only the first r left singular vectors of $\boldsymbol{U}$ with r typically being a much lower number compared to N. Based on Eq. (32) and the fact that $\boldsymbol{U}_r$ is unitary, a high-dimensional vector can be mapped into the latent subspace with its transpose:

$$\vec{c}_r = \boldsymbol{U}_r^T \vec{s}\,. \tag{33}$$

At the same time, if we have coordinates in the latent space, we can use Eq. (32) to reconstruct the corresponding high-dimensional vector (inverse mapping).

3. The only remaining piece that needs to be determined is the value of r. This can be done manually using a sensitivity study or by utilizing the singular values located on the diagonal

of matrix $\mathbf{\Sigma}$. The second approach is often referred to as energy-retention-based mode number determination that chooses r such that

$$r = \underset{1 \leq r \leq N_s}{\arg\min} \left(1 - \frac{\sum_{i=1}^{r} \sigma_i^2}{\sum_{i=1}^{N_s} \sigma_i^2} \right) < \tau \,, \tag{34}$$

where σ_i denotes the i-th singular value and τ is a filtering parameter (usually set to a small number). It can be shown [46] that if r is selected using this approach, the maximum relative discrete L2 error of the reconstructed high-dimensional vector (see Eq. (32)) over the data set (snapshots) is not larger than τ.

Once the POD modes are available, we can use them to map the already available snapshots into the latent space using Eq. (33). The coefficients of the snapshots in the latent space can then be used as training data for fitting Reduced-Order Models (ROMs). In this section, we use a polynomial regression-based ROM for verification purposes, while in Section 4.3, a multi-output Gaussian Process is used.

4.2.2 Implementation details

For performing the steps mentioned in the previous section, the MOOSE [40] framework and the Stochastic Tools Module (STM) [47] have been extended with various new, user-facing objects. The implementation relies heavily on the `MuliApp` system, meaning that a MOOSE-based app (main app) manages the runs of other MOOSE-based apps and collects information (snapshots in our case) from them. The application on the top is often referred to as the main application, whereas the underlying worker applications are called subapps. In this case the main application will sample input parameters for simulations, insert the parameter combinations into the numerical models in the corresponding subapps, run them and gather the snapshots. For this, the `Samplers` and `SamplerMultiApps` of STM are used. The storage and management of the high-dimensional vectors, however, is performed by newly added objects:

- `SolutionContainer`: Used for storing distributed solution/auxiliary system vectors. This container lives on a subapp and provides an interface for the main app when it comes to gathering solution fields.
- `ParallelSolutionStorage`: Stores multiple vectors on the main application. The vectors are organized based on solution/auxiliary variable names in a distributed fashion. The distribution is vector-based meaning that different vectors might belong to different processors, but entries of the same vector always belong to the same processor.
- `SerializedSolutionTransfer`: Extracts solution variable-based vectors from the `SolutionContainers` on the subapp and populates `ParallelSolutionStorage` with the data.

- `PODMapping`: Responsible for extracting the POD modes from the data stored in `ParallelSolutionStorage` using iterative SVD (see Eq. (31)) algorithms. This heavily relies on the Lánczos method-based SVD implemented in SLEPc [48]. Furthermore, this object executes the logic for selecting an adequate number of retained POD bases (r).
- `MappingReporter`: Uses Eq. (33) to project high-dimensional vectors to the latent space and stores the resulting coefficient vectors. This can be used to map the already available vectors from `ParallelSolutionStorage` or to map new solution vectors from new simulations on the fly. One of the main uses of this object is to create low-dimensional input data (coefficient vectors) for ROM generation.
- `InverseMapping`: Uses Eq. (32) together with already available coefficient vectors to reconstruct full solution fields. These solution fields can then be used by different high-dimensional solvers. The object accepts coefficient vectors from two sources:

    1. Manually defined coefficient vectors. This is useful for the visualization of the POD modes by setting the corresponding entry to 1, while keeping every other at 0.
    2. The output of a surrogate model. As already mentioned, surrogate models (or ROMs) can be trained to predict the entries of the coefficient vector.

4.2.3 Verification using polynomial regression

For the verification of the POD algorithm, we chose a simple, one-dimensional ($x \in [0, 10]$) diffusion problem:

$$-\frac{\partial}{\partial x}\left(4\frac{\partial u}{\partial x}\right) = S, \quad \text{with} \quad u(0) = 0, \quad \text{and} \quad u(10) = u_b, \tag{35}$$

where u is the solution variable, $u_b \sim \mathcal{U}(0, 10)$ a random boundary value and $S \sim \mathcal{U}(0, 10)$ is a random source term. The analytic solution for this problem can be derived by integrating the equation and applying the boundary conditions:

$$u(x) = \frac{S}{8}x^2 + \left(\frac{u_b}{10} + \frac{10S}{8}\right)x. \tag{36}$$

The analytic solution is a quadratic polynomial with the coefficients linearly depending on u_b and S. Without going into the detailed proofs of the claims below, we see that the analytic solution implies three things:

1. Since the analytic solution has two basis functions (x^2,x), we expect to get two POD modes as well. One can think about the POD modes as another basis for the same space with special requirements. Therefore, we can verify the implementation by only getting two basis functions from the snapshots.

2. Since the POD modes are constructed using the snapshots (linear combination of the snapshots), the first POD mode, which has a close correlation with the sample mean is expected to be a quadratic polynomial as well. This also implies that the second basis will be at most a quadratic polynomial. In other words, getting a quadratic and at most quadratic polynomial POD mode would verify our implementation.

3. Since the original expression shows an additive nature for (S and u_b) in terms of the expansion coefficients, the POD bases shall have expansion coefficients which depend linearly on these parameters. Therefore, we can verify the algorithm if we can fit linear functions for the expansion coefficients and reconstruct an unknown sample with an error of numerical roundoff.

As a first step, we verify if we obtain two POD modes only. For this, we sample 8 pairs of S and u_b using their corresponding distributions, solve Eq. (35) with each parameter combination, gather the solution vectors and extract the POD modes from the snapshots. Indeed, the only two POD modes correspond to non-zero singular values meaning that even though 8 snapshots are provided, all of them can be reconstructed using the 2 modes. These POD modes are presented in Figure 25. We see that both are quadratic functions which aligns with the second verification hypothesis.

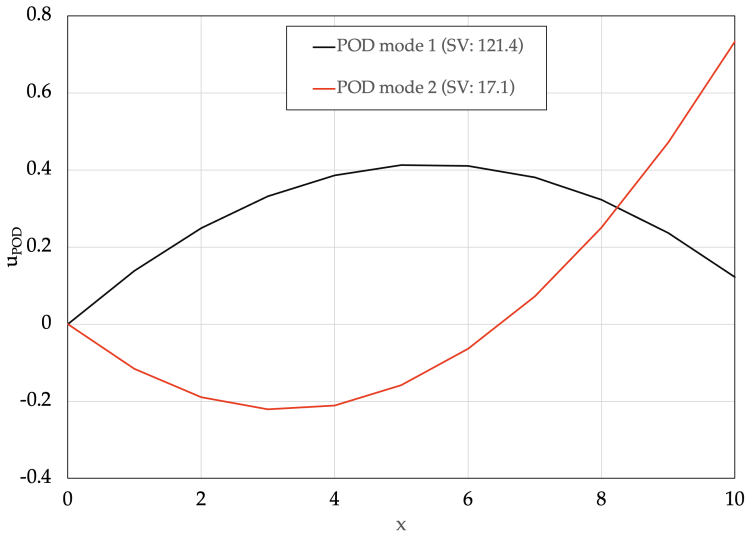

Figure 25: The two POD modes obtained from the one-dimensional verification example. The first mode (black) corresponds to a singular value of 121.4, while the second mode corresponds to a singular value of 17.1.

To verify the third statement, we map the 8 snapshots into the latent space using Eq. (33). Then two linear polynomials (having a form of $c_i(S, u_b) = p_i S + q_i u_b + l_i$) are fitted, one for each POD expansion coefficient. As a last step, a new input parameter combination ($S = 6.19$, $u_b = 3.12$) is selected and the corresponding POD expansion coefficients are computed by evaluating the linear polynomials. Using these POD expansion coefficients we reconstruct our solution using

Eq. (32) and compare it with the output of the high-dimensional model solved using the same input parameters. The comparison between the two fields yields $e_{L^2} = 2.55 \times 10^{-14}$ error which is considered roundoff verifying that the two quadratic POD modes combined with coefficients that are linear functions of S and u_b can reconstruct the exact solution.

4.2.4 Application to the Rosenthal temperature field

As previously discussed in Section 3.2.1, the Rosenthal expression provides a way to approximate the temperature field of a melt pool. This expression, however, depends on input parameters such as absorbed power, thermal conductivity and velocity. As an exercise of for the dimensionality reduction of a multi-dimensional field, we create a latent space for the Rosenthal temperature field in a two-dimensional domain. For this, we collect snapshots of the temperature fields obtained with different parameter combinations in the Rosenthal expression when the heat source reaches the middle point of the domain. Three parameters were chosen to be uncertain/changeable in the expression. These parameters together with their distributions for the random sampling are summarized in Table 3. We note that the heat source Q in Eq. (26) can be computed as the product of the absorptivity and the laser power ($Q = \eta P$).

Table 3: The distribution of the input parameters used for the stochastic evaluation of the Rosenthal expression.

Parameters	Distribution
Speed (v)	$\mathcal{U}(0.025,\ 0.05)\ \left(\frac{m}{s}\right)$
Absorptivity (η)	$\mathcal{U}(0.5,\ 1.5)\ (-)$
Laser Power (P)	$\mathcal{U}(500,\ 1500)\ (W)$

Using these distributions, 100 parameter combinations were sampled. Once the expression is evaluated at each parameter combination, the high-dimensional temperature fields are gathered and the POD modes are extracted. The decay in the normalized (by the sum, see Eq. (34)) singular values of the temperature is presented in Figure 26. We see that truncating the expansion by using only 5 POD modes would represent more than 99% of the variation in the system.

Using the inverse mapping capabilities in MOOSE, we can visualize the POD modes themselves as well. Figure 27 shows the first three POD modes which represent the most variation in the system. We see that the first mode (top) is close to an average temperature profile, while the second (middle) and third (bottom) modes describe the variation in the front and wake of the heat source.

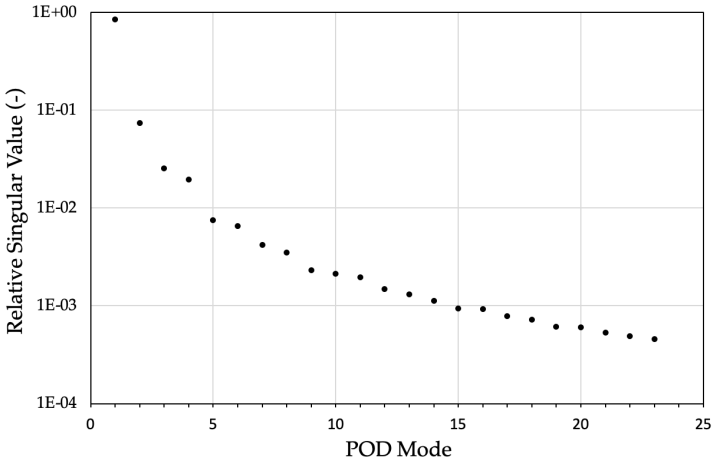

Figure 26: The decay of the normalized singular values obtained by the SVD of the snapshot matrix created using the Rosenthal temperature fields.

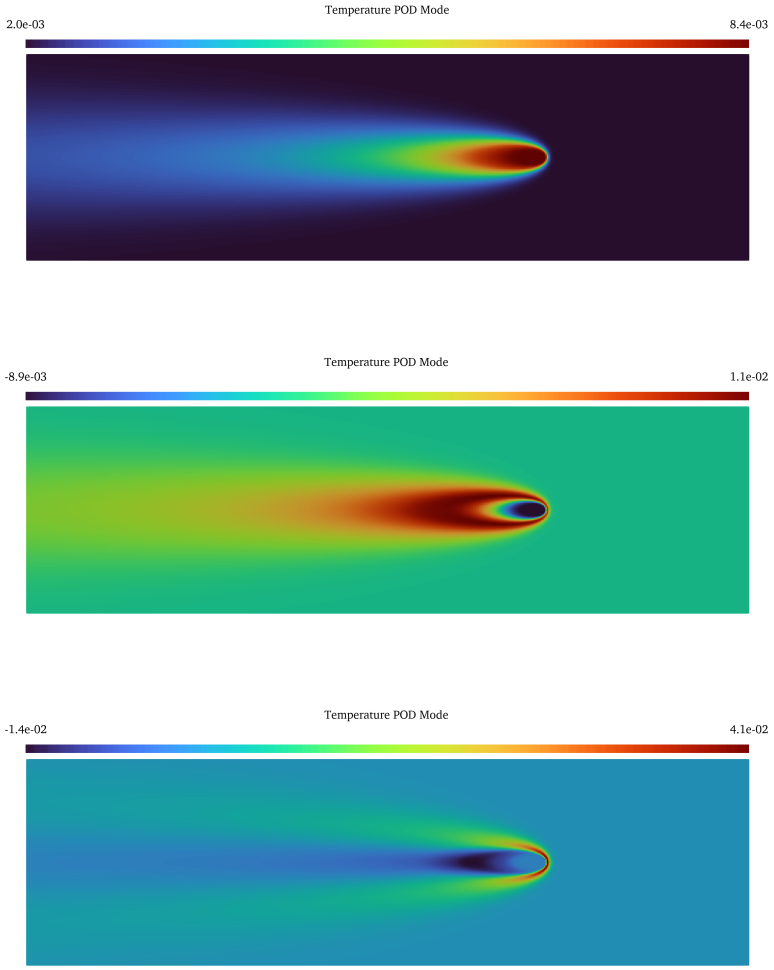

Figure 27: The first three (from top to bottom) POD modes of the Rosenthal temperature field with the varying input parameters.

4.3 Multi Output Gaussian Process

This section outlines the developments pertaining to the use of multi-output Gaussian processes (MOGPs) to efficiently and accurately predict the temperature fields during the additive manufacturing process. A theoretical background and the algorithmic implementation of MOGPs is first provided. Then, the effectiveness of MOGPs to predict the temperature fields is evaluated. Finally, ongoing implementations of MOGPs in the MOOSE stochastic tools module (STM) is discussed.

4.3.1 Theory

The theoretical background of MOGPs, starting with scalar Gaussian processes (GPs), is discussed below.

Scalar GPs

GPs approximate the function $f(\boldsymbol{x})$ using a Gaussian distribution in the form of:

$$\begin{aligned} f(\boldsymbol{x}) &= \mathcal{N}\Big(m(\boldsymbol{x}), \kappa(\boldsymbol{x}, \boldsymbol{x}')\Big) \\ m(\boldsymbol{x}) &= \mathbb{E}[f(\boldsymbol{x})] \\ \kappa(\boldsymbol{x}, \boldsymbol{x}') &= \mathbb{E}\Big[\Big(f(\boldsymbol{x}) - m(\boldsymbol{x})\Big)\ \Big(f(\boldsymbol{x}') - m(\boldsymbol{x}')\Big)\Big] \end{aligned} \tag{37}$$

where, $\boldsymbol{x}$ is the input vector, $m(\boldsymbol{x})$ is the mathematical expectation of $f(\boldsymbol{x})$, and $\kappa(\boldsymbol{x}, \boldsymbol{x}')$ is the kernel function that defines the covariance between $\boldsymbol{x}$ and a neighboring location $\boldsymbol{x}'$. The function $f(\boldsymbol{x})$ can be the scalar quantity of interest from a computational model or observed experimental data. If we have N scalar observations, they jointly follow a Gaussian distribution defined as [49, 50]:

$$\begin{aligned} \boldsymbol{y} &= [f(\boldsymbol{x}_1),\ f(\boldsymbol{x}_2), \ldots,\ f(\boldsymbol{x}_N)]^\intercal \sim \mathcal{N}(\boldsymbol{\mu},\ \boldsymbol{K}) \\ \boldsymbol{\mu} &= \Big[\mathbb{E}[f(\boldsymbol{x}_1)],\ \mathbb{E}[f(\boldsymbol{x}_2)], \ldots,\ \mathbb{E}[f(\boldsymbol{x}_N)]\Big]^\intercal \\ \boldsymbol{K}_{ij} &= \kappa(\boldsymbol{x}_i, \boldsymbol{x}_j) \end{aligned} \tag{38}$$

where, $\boldsymbol{\mu}$ is the mean vector and $\boldsymbol{K}$ is the covariance matrix. An element $\boldsymbol{K}_{ij}$ of $\boldsymbol{K}$ defines the covariance function or kernel function between $\boldsymbol{x}_i$ and $\boldsymbol{x}_j$. A popular kernel function used for setting up the covariance matrix $\boldsymbol{K}$ is the squared exponential kernel:

$$\kappa(\boldsymbol{x}, \boldsymbol{x}') = \sigma^2\ \exp\left(-\frac{1}{2}\sum_{d=1}^{D}\frac{(x_d - x'_d)^2}{l_d^2}\right) \tag{39}$$

, where σ^2 is the amplitude parameter and l_d is the length scale for input dimension d, and D is the number of input dimensions. Herein, we will use GPs and MOGPs to model the response of a computational model whose data is not corrupted by random noise. As such, the noise variance term which is commonly modeled using GPs and MOGPs, is ignored. Overall, a GP with the squared exponential kernel requires the specification of $D + 1$ hyper-parameters; that is, D length

scales and the amplitude parameter. For complex problems, these hyper-parameters are usually obtained by optimizing the log-likelihood function. In a GP, owing to the Gaussianity, the log-likelihood function has a closed form expression as shown below:

$$\mathcal{L} = -\frac{1}{2}\ \ln|\boldsymbol{K}| - \frac{1}{2}\,\boldsymbol{y}^T\,\boldsymbol{K}^{-1}\,\boldsymbol{y} - \frac{1}{2}\,N\ \ln(2\pi) \tag{40}$$

The log-likelihood function is constructed from the training data of model outputs vector $\boldsymbol{y}$ and the inputs $[\boldsymbol{x}_1, \boldsymbol{x}_2, \ldots,\ \boldsymbol{x}_N]$.

MOGPs

MOGPs model and predict the outputs which are vectors, each of size M. For any input vector $\boldsymbol{x}_i$, the vector of outputs $\boldsymbol{y}_i$ and the matrix of N vectors $\bar{\boldsymbol{Y}}$ is defined as:

$$\begin{aligned} \boldsymbol{y}_i &= [f(\boldsymbol{x}_i)^1,\ f(\boldsymbol{x}_i)^2, \ldots,\ f(\boldsymbol{x}_i)^M]^\intercal \\ \bar{\boldsymbol{Y}} &= [\boldsymbol{y}_1,\ \boldsymbol{y}_2, \ldots,\ \boldsymbol{y}_N]^\intercal \end{aligned} \tag{41}$$

where, $\boldsymbol{y}_i$ is of size $M \times 1$ and $\bar{\boldsymbol{Y}}$ is of size $N \times M$. The matrix $\bar{\boldsymbol{Y}}$ is vectorized and represented as $\hat{\boldsymbol{y}}$ with size $NM \times 1$. $\hat{\boldsymbol{y}}$ is modeled as a Gaussian distribution defined as:

$$\hat{\boldsymbol{y}} \sim \mathcal{N}\left(\hat{\boldsymbol{\mu}},\ \bar{\boldsymbol{K}}\right) \tag{42}$$

where, $\hat{\boldsymbol{\mu}}$ is the mean vector and $\bar{\boldsymbol{K}}$ is the full covariance matrix. $\bar{\boldsymbol{K}}$ captures covariances across the input variables and the vector of outputs and hence has size $NM \times NM$. $\bar{\boldsymbol{K}}$ can be modeled in several ways as discussed in [51, 52]. We will follow the linear model of co-regionalization (LMC) which distinctly models the covariances between the N inputs and the M outputs. Mathematically, the LMC is defined as [51, 53]:

$$\bar{\boldsymbol{K}} = \sum_{q=1}^{Q} \bar{\boldsymbol{B}}_q \otimes \boldsymbol{K}_q \tag{43}$$

where, q denotes the basis index, $\bar{\boldsymbol{B}}_q$ output covariance matrix of size $M \times M$ for the q^{th} covariate, $\boldsymbol{K}_q$ is the inputs covariance matrix of size $N \times N$ for the q^{th} covariate, Q is the total number of basis, and $\otimes$ denotes the Kronecker product. $\bar{\boldsymbol{B}}_q$ is further defined as the sum of two matrices of weights [53]:

$$\bar{\boldsymbol{B}}_q = \boldsymbol{A}_q \boldsymbol{A}_q^\intercal + \text{diag}\left(\boldsymbol{\lambda}_q\right) \tag{44}$$

where, $\boldsymbol{A}_q$ and $\boldsymbol{\lambda}_q$ are the matrix (size $M \times R$) and vector (size $M \times 1$) of hyper-parameters, both for the q^{th} basis. The size R is user-defined and it can greater than or equal to 1. The larger the R, the more sophisticated the MOGP in modeling complex outputs. Specifically, $\boldsymbol{A}_q$ is defined as:

$$\boldsymbol{A}_q = \begin{bmatrix} a_{q,11} & \dots & a_{q,1R} \\ \vdots & \ddots & \vdots \\ a_{q,M1} & \dots & a_{q,MR} \end{bmatrix} \tag{45}$$

In addition, the size of Q can also be greater than or equal to 1. The larger the Q, the more sophisticated the MOGP in modeling complex outputs. For every $q \in \{1, \dots, Q\}$, a separate $\boldsymbol{A}_q$ matrix, $\boldsymbol{\lambda}_q$ vector, and $\boldsymbol{K}_q$ matrix is defined. Each of the $\boldsymbol{K}_q$ matrices can be defined by the same or different covariance kernels and have separate hyper-parameters. We will use the same covariance kernel, the squared exponential kernel defined in Equation (39), for every q. In total, the MOGP with the LMC output covariance and the squared exponential input covariance kernel will have $Q\ (D+1)\ (M+1)\ R$ hyper-parameters to be optimized arising from Q basis. If $Q = 1$, the LMC reduces to the intrinsic co-regionalization model (ICM) with $(D+1)\ (M+1)\ R$ hyper-parameters to be optimized. Table 4 summarizes the vectors and matrices used in MOGPs with their sizes.

Table 4: A summary of the vectors and matrices used in MOGPs with their sizes. N is the number of inputs and M is the number of outputs for each input.

Notation	Size	Description
$\boldsymbol{y}_i$	$M \times 1$	i^{th} output vector
$\bar{\boldsymbol{Y}}$	$N \times M$	Output matrix
$\hat{\boldsymbol{y}}$	$NM \times 1$	Output vector
$\hat{\boldsymbol{\mu}}$	$NM \times 1$	Mean vector
$\bar{\boldsymbol{K}}$	$NM \times NM$	Full covariance matrix
$\bar{\boldsymbol{B}}_q$	$M \times M$	Output covariance matrix
$\boldsymbol{K}_q$	$N \times N$	Input covariance matrix
$\boldsymbol{A}_q$	$M \times R$	Weight matrix for q^{th} basis
$\boldsymbol{\lambda}_q$	$M \times 1$	Intra-covariate weights for q^{th} basis

4.3.2 Hyper-parameter optimization using AdamW

The hyper-parameters of the MOGP model are inferred by optimizing the log-likelihood function. The MOGP log-likelihood function has a form similar to a scalar GP:

$$\mathcal{L} = -\frac{1}{2}\ \ln|\bar{\boldsymbol{K}}| - \frac{1}{2}\,\hat{\boldsymbol{y}}^T\,\bar{\boldsymbol{K}}^{-1}\,\hat{\boldsymbol{y}} - \frac{1}{2}\,N\ \ln(2\pi) \tag{46}$$

We will use the adaptive moment estimation (Adam) algorithm to optimize the MOGP hyper-parameters [54]. Adam is a stochastic optimization algorithm that permits mini-batch sampling during the optimization iterations. The optimization of MOGPs can be expensive. If there are N training points each with M outputs, each training iteration of Adam has a cost of $\mathcal{O}(M^3N^3)$. Adam permits using $n < N$ random training points during each iteration which has a cost of $\mathcal{O}(M^3n^3) << \mathcal{O}(M^3N^3)$. Recently, [55] proposed the AdamW algorithm which modifies how

the regularization is performed in Adam, increasing its optimization performance. In traditional Adam with regularization, the gradient update and hyper-parameter update steps are defined as [54]:

$$\begin{aligned} \boldsymbol{g}_t &\leftarrow \nabla \mathcal{L}_t(\boldsymbol{\theta}_{t-1}) + \lambda\, \boldsymbol{\theta}_{t-1} \\ \boldsymbol{\theta}_t &\leftarrow \boldsymbol{\theta}_{t-1} - \eta_t \Big(\alpha \hat{\boldsymbol{m}}_t / (\sqrt{\hat{\boldsymbol{v}}_t} + \varepsilon) \Big) \end{aligned} \tag{47}$$

where, t is the iteration, $\boldsymbol{\theta}$ is the optimizable hyper-parameters, $\boldsymbol{g}$ is the gradient update, λ is the regularization weight, α and ε are internal parameters of the algorithm, $\hat{\boldsymbol{m}}$ is the corrected first moment update, $\hat{\boldsymbol{v}}$ is the corrected second moment update, and η is the schedule multiplier. AdamW modifies the gradient update and hyper-parameter update steps as follows [55]:

$$\begin{aligned} \boldsymbol{g}_t &\leftarrow \nabla f_t(\boldsymbol{\theta}_{t-1}) \\ \boldsymbol{\theta}_t &\leftarrow \boldsymbol{\theta}_{t-1} - \eta_t \Big(\alpha \hat{\boldsymbol{m}}_t / (\sqrt{\hat{\boldsymbol{v}}_t} + \varepsilon) + \lambda\, \boldsymbol{\theta}_{t-1} \Big) \end{aligned} \tag{48}$$

wherein, it is noticed that the regularization is decoupled from the gradient update step and added to the hyper-parameter update step. [55] found that this de-coupling leads to better performance of the Adam algorithm in general across a suite of case studies that were considered. We will use the AdamW optimizer to infer the MOGP hyper-parameters with the schedule multiplier η set to 1.0.

Forward prediction and uncertainty quantification

Once the MOGP hyper-parameters are optimized, probabilistic predictions of the vector quantities of interest can be made. Given a prediction input $\boldsymbol{x}_*$, the probability distribution of the vector outputs is given by:

$$p(\hat{\boldsymbol{y}}_* | \boldsymbol{x}_*, \hat{\boldsymbol{y}}, \bar{\boldsymbol{x}}, \boldsymbol{\theta}) = \mathcal{N}(\hat{\boldsymbol{\mu}}_*,\, \bar{\boldsymbol{\Sigma}}_*) \tag{49}$$

where, $\bar{\boldsymbol{x}}$ is the matrix of training inputs, $\hat{\boldsymbol{\mu}}_*$ is the mean vector, and $\bar{\boldsymbol{\Sigma}}_*$ is the covariance matrix. The mean vector is defined as:

$$\hat{\boldsymbol{\mu}}_* = \bar{\boldsymbol{K}}_{\hat{\boldsymbol{y}}_*, \hat{\boldsymbol{y}}} \left(\bar{\boldsymbol{K}}_{\hat{\boldsymbol{y}}, \hat{\boldsymbol{y}}} \right)^{-1} \hat{\boldsymbol{y}} \tag{50}$$

where, $\bar{\boldsymbol{K}}_{\hat{\boldsymbol{y}}_*, \hat{\boldsymbol{y}}}$ is the full covariance matrix of the training inputs and prediction inputs and $\bar{\boldsymbol{K}}_{\hat{\boldsymbol{y}}, \hat{\boldsymbol{y}}}$ is the full covariance matrix of the training inputs. The covariance matrix $\bar{\boldsymbol{\Sigma}}_*$ is defined as:

$$\bar{\boldsymbol{\Sigma}}_* = \bar{\boldsymbol{K}}_{\hat{\boldsymbol{y}}_*, \hat{\boldsymbol{y}}_*} - \bar{\boldsymbol{K}}_{\hat{\boldsymbol{y}}_*, \hat{\boldsymbol{y}}} \left(\bar{\boldsymbol{K}}_{\hat{\boldsymbol{y}}, \hat{\boldsymbol{y}}} \right)^{-1} \bar{\boldsymbol{K}}_{\hat{\boldsymbol{y}}_*, \hat{\boldsymbol{y}}}^{\intercal} \tag{51}$$

where, $\bar{\boldsymbol{K}}_{\hat{\boldsymbol{y}}_*, \hat{\boldsymbol{y}}_*}$ is the full covariance matrix of the prediction inputs.

4.3.3 Implementation in MOOSE Stochastic Tools Module

The MOGP capabilities are being implemented and tested in the MOOSE STM [47]. This section outlines the framework for implementing MOGPs in the STM. It consists of five new objects whose function is discussed below:

`MultiOutputGaussianProcessTrainer`: This object gathers the training inputs and outputs which are both vectors from the sub-application. It prepares the training data by performing standardization. It then sends this data to the MOGP optimizer.

`Standardizer`: New functions are being implemented in this object to permit performing standardization while accounting for the covariances in the training data. This is particularly important for MOGPs wherein the output data is correlated.

`OutputCovariance`: This new object considers the covariances between the outputs and its derived classes lets users implements covariance models like the ICM and LMC.

`MultiOutputGaussianProcessHandler`: This utility object performs the hyper-parameter optimization of the MOGP. It takes training data from the `MultiOutputGaussianProcessTrainer` and information of the input and output covariances from `Covariance` and `OutputCovariance`, respectively. It uses the AdamW optimizer to tune the MOGP hyper-parameters.

`MultiOutputGaussianProcess`: Once the MOGP hyper-parameters are tuned, this object makes the predictions of the field quantity of interest for a testing dataset.

4.3.4 Application to Rosenthal temperature field prediction (MOGPs + POD)

The MOGPs are applied to predict the stationary temperature distribution in the domain during the additive manufacturing process. We will rely on the Rosenthal equation for generating the training and testing data of the temperature distributions. In the domain, we are interested in predicting the temperature spatial distribution at 100×100 locations on the Z-plane. This amounts to predicting a vector of $10,000$ temperature values using MOGPs. The training of the MOGPs, as discussed earlier, is very expensive and each training iteration is of the cost $\mathcal{O}(N^3M^3)$. If $M = 10,000$, the training cost can blow up. To alleviate this issue and to increase the effectiveness of the MOGP, we will apply POD to the training data, train the MOGP in the latent space with smaller dimension m ($m << M$), make MOGP predictions in the latent space, and transform the predictions made into the required space.

We generated 200 training data sets of input variables like ambient temperature, absorptivity, laser power, conductivity, and laser velocity and output temperatures at the $10,000$ locations. We then performed POD on the output temperatures which is very high dimensional. For each additional principal component of the POD analysis, we computed the explained variance ratio. Figure 28a presents the explained variance ratio as a function of the principal component index. It is noted that the explained variance ratio rapidly diminishes as the number of principal

components increases. Figure 28b presents the cumulative explained variance ratio as a function of the principal component index. As we consider 2 or more principal components, the cumulative explained variance ratio is almost equal to one. This indicates that the very high-dimensional temperature outputs can be succinctly represented by two principal components (i.e., latent variables).

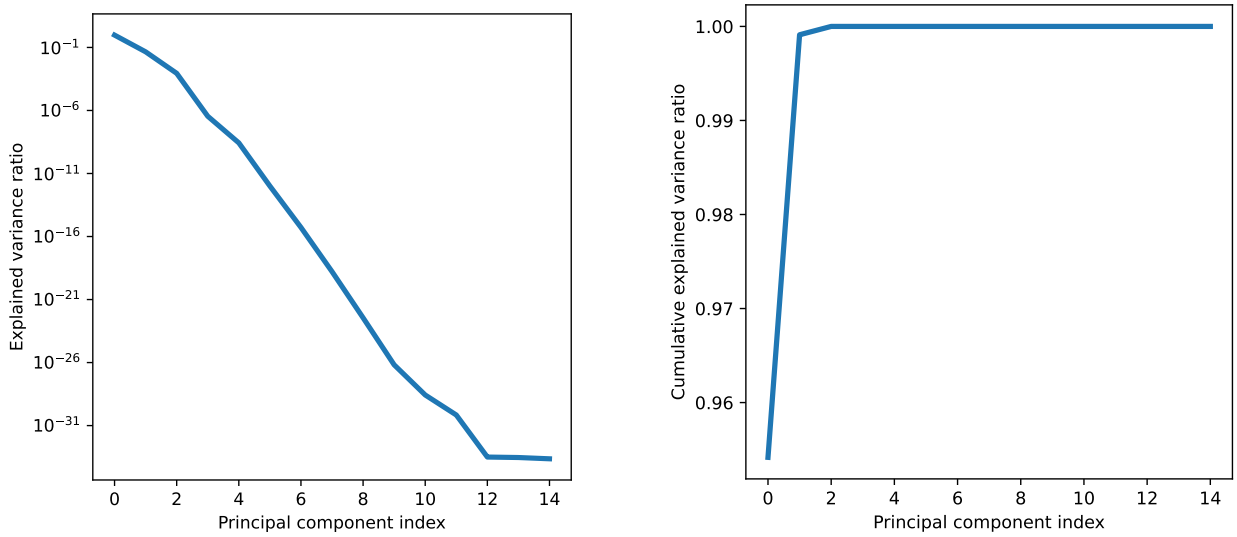

(a) (b)

Figure 28: (a) The explained variance ratio as a function of the principal component index and (b) the cumulative explained variance ratio as a function of the principal component index for the temperature spatial distribution.

After downsizing the high-dimensional output temperatures to two principal components, training of the MOGP is performed with the 200 training data points. The MOGP is designed to have the output covariance described by the ICM with $R = 1$ set in the $\boldsymbol{A}_q$ matrix. This will result in 9 MOGP hyper-parameters considering that $D = 5$. Optimization of these hyper-parameters is performed using AdamW with the number of iterations as 4,000, learning rate as $5E-4$, and $\lambda = 1E-4$. Figure 29 presents the evolution of the loss function or the log-likelihood function as a function of the iterations. The stochasticity in the loss function evolution is due to the mini-batch sampling with the batch size set to 50. It is observed that as the number of iterations increase, the loss function is reduced to an almost constant value, representing the tuning of the MOGP hyper-parameters.

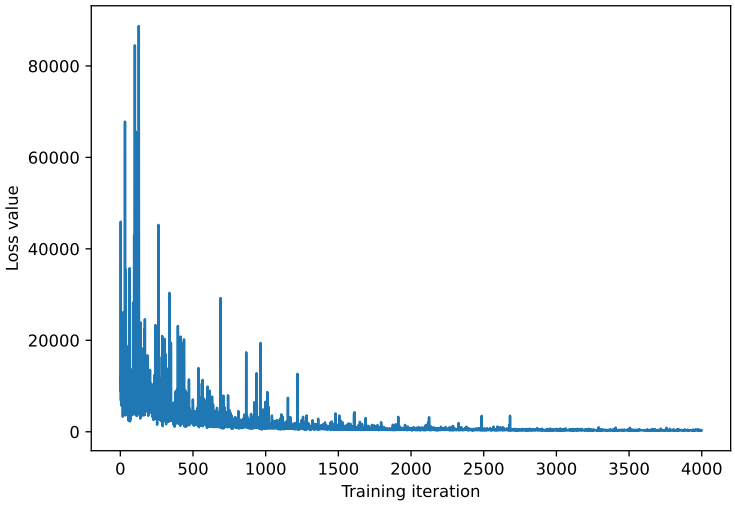

Figure 29: Loss function evolution of the MOGP with the optimization iterations. It is observed that as the number of iterations increase, the loss function is reduced to an almost constant value, representing the tuning of the MOGP hyper-parameters.

Once the MOGP hyper-parameters are optimized, its performance is tested on a testing dataset. Figure 30 presents the performance of the MOGP for two representative testing inputs. Figures 30a and 30b show the MOGP mean temperature predictions, Figures 30c and 30d show the MOGP predictive standard deviation (which represents the uncertainties in the predictions), and Figures 30e and 30f show the "true" or reference temperature distribution. It observed that the mean MOGP predictions of the temperature distribution closely match the "true" solution. Moreover, the predictive standard deviation of MOGP is small compared to magnitude of the temperatures. These initial results demonstrate that the MOGP is effective at predicting field quantities like temperature during the AM process. One more advantages of an MOGP is that it comes with predictive uncertainties which can be leveraged in active learning frameworks.

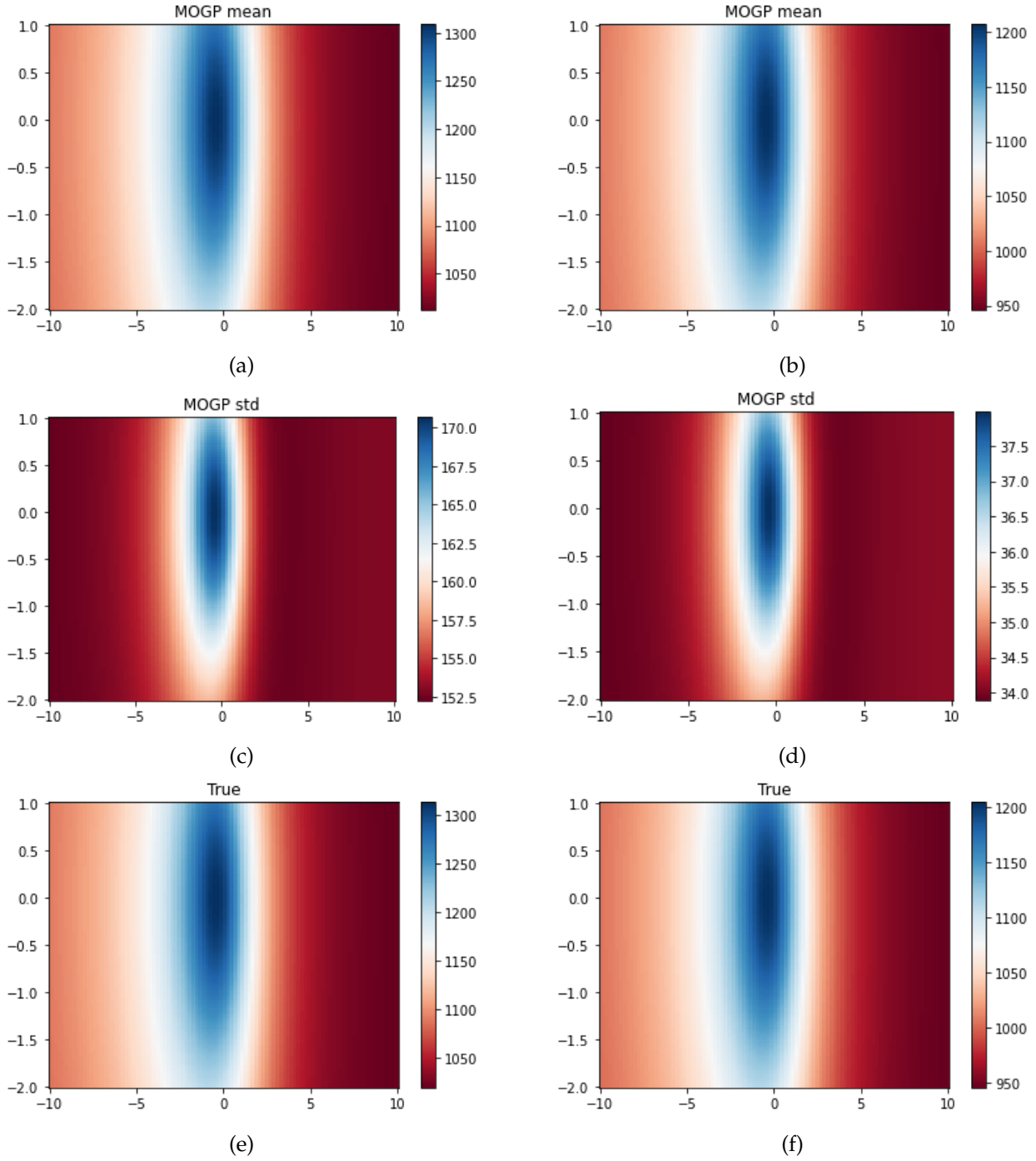

Figure 30: (a) and (b) MOGP mean predictions; (c) and (d) MOGP predictive standard deviations; and (e) and (f) the "true" solution of the temperature distribution for two testing points. (a), (c), and (e) correspond to testing point 1. (b), (d), and (f) correspond to testing point 2.

5. Conclusion

In conclusion, we develop various physics-based and Machine learning models to connect the process conditions to the microstructural evolution of 316 SS during LPBF process. We demonstrate the capabilities of MALMUTE to capture the complex physics aspects of the LPBF process. Furthermore, a Proper Orthogonal Decomposition (POD)-based dimensionality reduction has been implemented in MOOSE. It provides algorithms for extracting feature vectors from fields of interest which can be used for mapping high-dimensional fields to lower dimensional latent spaces. This mapping can be also used in combination with surrogate models (such as MOGPs) to create estimators for entire field quantities with a fraction of the simulation time that would be otherwise required. MOGPs were tested for accelerating the prediction of field quantities like temperature during the AM process. For a representative AM example, MOGPs using the ICM covariance model combined with PODs showed good performance in predicting the temperature distributions. Furthermore, the implementation of MOGPs in MOOSE STM is currently being pursued.

This work aims to develop the computational framework necessary for capturing different aspects of the AM process and associated microstructural evolution. It lays the foundation for reaching the overall goal of establishing a reduced-order PSPP correlation for AM materials. The generated models can also be used within an active learning framework to identify data need for accelerated material development and qualification for AMMT program.

REFERENCES

[1] A. Simchi, Direct laser sintering of metal powders: Mechanism, kinetics and microstructural features, Materials Science and Engineering: A 428 (1) (2006) 148–158. doi:https://doi.org/10.1016/j.msea.2006.04.117.
URL https://www.sciencedirect.com/science/article/pii/S0921509306005491

[2] J. Liu, Y. Song, C. Chen, X. Wang, H. Li, C. Zhou, J. Wang, K. Guo, J. Sun, Effect of scanning speed on the microstructure and mechanical behavior of 316l stainless steel fabricated by selective laser melting, Materials Design 186 (2020) 108355. doi:https://doi.org/10.1016/j.matdes.2019.108355.
URL https://www.sciencedirect.com/science/article/pii/S0264127519307932

[3] R. Chai, Y. Zhang, B. Zhong, C. Zhang, Effect of scan speed on grain and microstructural morphology for laser additive manufacturing of 304 stainless steel, REVIEWS ON ADVANCED MATERIALS SCIENCE 60 (1) (2021) 744–760 [cited 2023-09-28]. doi:doi:10.1515/rams-2021-0068.
URL https://doi.org/10.1515/rams-2021-0068

[4] A. Röttger, K. Geenen, M. Windmann, F. Binner, W. Theisen, Comparison of microstructure and mechanical properties of 316l austenitic steel processed by selective laser melting with hot-isostatic pressed and cast material, Materials Science and Engineering: A 678 (2016) 365–376. doi:https://doi.org/10.1016/j.msea.2016.10.012.
URL https://www.sciencedirect.com/science/article/pii/S0921509316312205

[5] P. Promoppatum, R. Onler, S.-C. Yao, Numerical and experimental investigations of micro and macro characteristics of direct metal laser sintered ti-6al-4v products, Journal of Materials Processing Technology 240 (2017) 262–273. doi:https://doi.org/10.1016/j.jmatprotec.2016.10.005.
URL https://www.sciencedirect.com/science/article/pii/S0924013616303545

[6] A. Lindsay, R. Stogner, D. Gaston, D. Schwen, C. Matthews, W. Jiang, L. K. Aagesen, R. Carlsen, F. Kong, A. Slaughter, et al., Automatic differentiation in metaphysicl and its applications in moose, Nuclear Technology 207 (7) (2021) 905–922.

[7] C. Sun, Y. Wang, M. D. McMurtrey, N. D. Jerred, F. Liou, J. Li, Additive manufacturing for energy: A review, Applied Energy 282A (116041).

[8] M. McMurtrey, R. O'Brien, C. Sun, C.-H. Shiau, F. Teng, Irradiation damage and iascc of printed 316l for use as fuel cladding, in: 19th International Conference on Environmental Degradation of Materials in Nuclear Power Systems - Water Reactors, Boston, MA, USA, 2019.

[9] M. McMurtrey, C. Sun, R. Rupp, C.-H. Shiau, R. Hanbury, N. Jerred, R. O'Brien, Investigation of the irradiation effects in additively manufactured 316l steel resulting in decreased irradiation assisted stress corrosion cracking susceptibility, Journal of Nuclear Materials 545 (2021) 152739.

[10] M. Song, M. Wang, X. Lou, R. Rebak, G. Was, Radiation damage and irradiation-assisted stress corrosion cracking of additively manufactured 316l stainless steels, Journal of Nuclear Materials 513 (2019) 33–44.

[11] M. McMurtrey, M. Messner, Qualification challenges for additive manufacturing in high temperature nuclear applications, in: the ASME 2021 Pressure Vessels & Piping Conference, PVP 2021, 2021.

[12] M. Bayant, W. Dong, J. Thorborg, A. C. To, J. H. Hattel, A review of multi-scale and multi-physics simulations of metal additive manufacturing processes with focus on modeling strategies, Additive Manufacturing 47 (102278).

[13] M. M. Francois, A. Sun, et al., Modeling of additive manufacturing processes for metals: Challenges and opportunities, Current Opinion in Solid State Materials Science 21 (2017) 198–206.

[14] Z. Jin, Z. Zhang, K. Demir, G. X. Gu, Machine learning for advanced additive manufacturing, Matter 3 (2020) 1541–1556.

[15] P. C. Collins, C. V. Haden, I. Ghamarian, et al., Progress towards an integration of process-structure-property-performance models for three-dimensional (3-d) printing of titanium alloys, JOM 66 (2014) 1299–1309.

[16] I. Gibson, D. Rosen, B. Stucker, Additive Manufacturing Technologies.

[17] D. Svetlizky, M. Das, B. Zheng, A. L. Vyatskikh, S. Bose, A. Bandyopadhyay, J. M. Schoenung, E. J. Lavernia, N. Eliaz, Directed energy deposition (ded) additive manufacturing: Physical characteristics, defects, challenges and applications, Materials Today 49 (2021) 271–295. doi:https://doi.org/10.1016/j.mattod.2021.03.020.
URL https://www.sciencedirect.com/science/article/pii/S1369702121001139

[18] K. Amato, S. Gaytan, L. Murr, E. Martinez, P. Shindo, J. Hernandez, S. Collins, F. Medina, Microstructures and mechanical behavior of inconel 718 fabricated by selective laser melting, Acta Materialia 60 (5) (2012) 2229–2239. doi:https://doi.org/10.1016/j.actamat.2011.12.032.
URL https://www.sciencedirect.com/science/article/pii/S1359645411008949

[19] G. Miranda, S. Faria, F. Bartolomeu, E. Pinto, S. Madeira, A. Mateus, P. Carreira, N. Alves, F. Silva, O. Carvalho, Predictive models for physical and mechanical properties of 316l

stainless steel produced by selective laser melting, Materials Science and Engineering: A 657 (2016) 43–56. doi:https://doi.org/10.1016/j.msea.2016.01.028.
URL https://www.sciencedirect.com/science/article/pii/S0921509316300272

[20] D. Kong, X. Ni, C. Dong, X. Lei, L. Zhang, C. Man, J. Yao, X. Cheng, X. Li, Bio-functional and anti-corrosive 3d printing 316l stainless steel fabricated by selective laser melting, Materials Design 152 (2018) 88–101. doi:https://doi.org/10.1016/j.matdes.2018.04.058.
URL https://www.sciencedirect.com/science/article/pii/S0264127518303368

[21] D. Wang, C. Song, Y. Yang, Y. Bai, Investigation of crystal growth mechanism during selective laser melting and mechanical property characterization of 316l stainless steel parts, Materials Design 100 (C) (2016) 291–299. doi:10.1016/j.matdes.2016.03.111.

[22] Y. Y. C. Choong, G. K. H. Chua, C. H. Wong, Investigation on the integral effects of process parameters on properties of selective laser melted stainless steel parts, in: Proceedings of the 3rd International Conference on Progress in Additive Manufacturing (Pro-AM 2018), 2018. doi:10.25341/D4P88S.

[23] J. Simmons, M. Daeumer, A. Azizi, Local thermal conductivity mapping of selective laser melted 316l stainless steel, in: Solid Freeform Fabrication 2018: Proceedings of the 29th Annual International Solid Freeform Fabrication Symposium – An Additive Manufacturing Conference), 2018, pp. 1–14. doi:http://dx.doi.org/10.26153/tsw/17161.

[24] E. Liverani, S. Toschi, L. Ceschini, A. Fortunato, Effect of selective laser melting (slm) process parameters on microstructure and mechanical properties of 316l austenitic stainless steel, Journal of Materials Processing Technology 249 (2017) 255–263. doi:https://doi.org/10.1016/j.jmatprotec.2017.05.042.
URL https://www.sciencedirect.com/science/article/pii/S0924013617302169

[25] T. R. Smith, J. D. Sugar, C. San Marchi, J. M. Schoenung, Strengthening mechanisms in directed energy deposited austenitic stainless steel, Acta Materialia 164 (2019) 728–740. doi:https://doi.org/10.1016/j.actamat.2018.11.021.
URL https://www.sciencedirect.com/science/article/pii/S1359645418308978

[26] Z. Zhang, B. Chu, L. Wang, Z. Lu, Comprehensive effects of placement orientation and scanning angle on mechanical properties and behavior of 316l stainless steel based on the selective laser melting process, Journal of Alloys and Compounds 791 (2019) 166–175. doi:https://doi.org/10.1016/j.jallcom.2019.03.082.
URL https://www.sciencedirect.com/science/article/pii/S0925838819308898

[27] P. Promoppatum, S.-C. Yao, P. C. Pistorius, A. D. Rollett, A comprehensive comparison of the analytical and numerical prediction of the thermal history and solidification microstructure of inconel 718 products made by laser powder-bed fusion, Engineering 3 (5) (2017) 685–694.

doi:https://doi.org/10.1016/J.ENG.2017.05.023.
URL https://www.sciencedirect.com/science/article/pii/S2095809917307208

[28] M. Sadowski, L. Ladani, W. Brindley, J. Romano, Optimizing quality of additively manufactured inconel 718 using powder bed laser melting process, Additive Manufacturing 11 (2016) 60–70. doi:https://doi.org/10.1016/j.addma.2016.03.006.
URL https://www.sciencedirect.com/science/article/pii/S2214860416300483

[29] L. Rickenbacher, T. Etter, S. Hövel, K. Wegener, High temperature material properties of in738lc processed by selective laser melting (slm) technology, Rapid Prototyping Journal 19 (4) (2013) 282–290. doi:https://doi.org/10.1108/13552541311323281.
URL https://www.emerald.com/insight/content/doi/10.1108/13552541311323281/full/html

[30] E. Chlebus, K. Gruber, B. Kuźnicka, J. Kurzac, T. Kurzynowski, Effect of heat treatment on the microstructure and mechanical properties of inconel 718 processed by selective laser melting, Materials Science and Engineering: A 639 (2015) 647–655. doi:https://doi.org/10.1016/j.msea.2015.05.035.
URL https://www.sciencedirect.com/science/article/pii/S0921509315005687

[31] S. Balay, S. Abhyankar, M. F. Adams, S. Benson, J. Brown, P. Brune, K. Buschelman, E. Constantinescu, L. Dalcin, A. Dener, V. Eijkhout, J. Faibussowitsch, W. D. Gropp, V. Hapla, T. Isaac, P. Jolivet, D. Karpeev, D. Kaushik, M. G. Knepley, F. Kong, S. Kruger, D. A. May, L. C. McInnes, R. T. Mills, L. Mitchell, T. Munson, J. E. Roman, K. Rupp, P. Sanan, J. Sarich, B. F. Smith, S. Zampini, H. Zhang, H. Zhang, J. Zhang, PETSc/TAO users manual, Tech. Rep. ANL-21/39 - Revision 3.19, Argonne National Laboratory (2023). doi:10.2172/1968587.

[32] A. Lindsay, G. Giudicelli, P. German, J. Peterson, Y. Wang, R. Freile, D. Andrs, P. Balestra, M. Tano, R. Hu, et al., Moose navier–stokes module, SoftwareX 23 (2023) 101503.

[33] S. Biswas, D. Liu, L. K. Aagesen, W. Jiang, Solidification and grain formation in alloys: a 2d application of the grand-potential-based phase-field approach, Modelling Simul. Mater. Sci. Eng. 30.

[34] D. R. Gaston, C. J. Permann, J. W. Peterson, A. E. Slaughter, D. Andrš, Y. Wang, M. P. Short, D. M. Perez, M. R. Tonks, J. Ortensi, L. Zou, R. C. Martineau, Physics-based multiscale coupling for full core nuclear reactor simulation, Annals of Nuclear Energy 84 (2015) 45–54.

[35] A. Dindale, Sgte data for pure elements, Calphad 15 (1991) 317–425.

[36] J. Miettinen, Thermodynamic reassessment of fe-cr-ni system with emphasis on the iron-rich corner., Calphad 23 (1999) 231–248.

[37] M. Plapp, Unified derivation of phase-field models for alloy solidification from a grand-potential functional, Physical Review E 84 (3) (2011) 031601.
URL <GotoISI>://WOS:000294569000002

[38] L. K. Aagesen, Y. Gao, D. Schwen, K. Ahmed, Grand-potential-based phase-field model for multiple phases, grains, and chemical components, Physical Review E 98 (2018) 023309.

[39] A. Chadwick, P. Voorhees, The development of grain structure during additive manufacturing, Acta Materialia 211.

[40] A. D. Lindsay, D. R. Gaston, C. J. Permann, J. M. Miller, D. Andrš, A. E. Slaughter, F. Kong, J. Hansel, R. W. Carlsen, C. Icenhour, L. Harbour, G. L. Giudicelli, R. H. Stogner, P. German, J. Badger, S. Biswas, L. Chapuis, C. Green, J. Hales, T. Hu, W. Jiang, Y. S. Jung, C. Matthews, Y. Miao, A. Novak, J. W. Peterson, Z. M. Prince, A. Rovinelli, S. Schunert, D. Schwen, B. W. Spencer, S. Veeraraghavan, A. Recuero, D. Yushu, Y. Wang, A. Wilkins, C. Wong, 2.0 - MOOSE: Enabling massively parallel multiphysics simulation, SoftwareX 20 (2022) 101202. doi:https://doi.org/10.1016/j.softx.2022.101202.
URL https://www.sciencedirect.com/science/article/pii/S2352711022001200

[41] L. Sirovich, Turbulence and the dynamics of coherent structures. i. coherent structures, Quarterly of applied mathematics 45 (3) (1987) 561–571.

[42] Y. Liang, H. Lee, S. Lim, W. Lin, K. Lee, C. Wu, Proper orthogonal decomposition and its applications—part i: Theory, Journal of Sound and vibration 252 (3) (2002) 527–544.

[43] S. Wold, K. Esbensen, P. Geladi, Principal component analysis, Chemometrics and intelligent laboratory systems 2 (1-3) (1987) 37–52.

[44] K. Fukunaga, W. L. Koontz, Application of the karhunen-loeve expansion to feature selection and ordering, IEEE Transactions on computers 100 (4) (1970) 311–318.

[45] G. W. Stewart, On the early history of the singular value decomposition, SIAM review 35 (4) (1993) 551–566.

[46] V. Klema, A. Laub, The singular value decomposition: Its computation and some applications, IEEE Transactions on automatic control 25 (2) (1980) 164–176.

[47] A. E. Slaughter, Z. M. Prince, P. German, I. Halvic, W. Jiang, B. W. Spencer, S. L. Dhulipala, D. R. Gaston, Moose stochastic tools: A module for performing parallel, memory-efficient in situ stochastic simulations, SoftwareX 22 (2023) 101345.

[48] V. Hernandez, J. E. Roman, V. Vidal, Slepc: A scalable and flexible toolkit for the solution of eigenvalue problems, ACM Transactions on Mathematical Software (TOMS) 31 (3) (2005) 351–362.

[49] C. K. Williams, C. E. Rasmussen, Gaussian processes for machine learning, MIT press, Cambridge, MA, 2006.

[50] S. L. N. Dhulipala, M. D. Shields, B. W. Spencer, C. Bolisetti, A. E. Slaughter, V. M. Labouré, P. Chakroborty, Active learning with multifidelity modeling for efficient rare event simulation, Journal of Computational Physics 468 (2022) 111506.

[51] H. Liu, J. Cai, Y. S. Ong, Remarks on multi-output gaussian process regression, Knowledge-Based Systems 144 (2018) 102–112.

[52] M. A. Alvarez, L. Rosasco, N. D. Lawrence, Kernels for vector-valued functions: A review, Foundations and Trends in Machine Learning 4 (3) (2012) 195–266.

[53] L. F. Cheng, B. Dumitrascu, G. Darnell, C. Chivers, M. Draugelis, K. Li, B. E. Engelhardt, Sparse multi-output gaussian processes for online medical time series prediction, BMC medical informatics and decision making 20 (1) (2020) 1–23.

[54] D. P. Kingma, J. Ba, Adam: A method for stochastic optimization, arXiv preprint arXiv:1412.6980.

[55] I. Loshchilov, F. Hutter, Decoupled weight decay regularization, arXiv preprint arXiv:1711.05101.